

3D Simulations of Strongly Magnetised Non-Rotating Supernovae: Explosion Dynamics and Remnant Properties

Vishnu Varma^{1,2*}, Bernhard Müller^{1†}, Fabian R. N. Schneider^{3,4}

¹ School of Physics and Astronomy, 10 College Walk, Monash University, Clayton, VIC 3800, Australia

² Astrophysics Group, Lennard-Jones Laboratories, Keele University, Keele ST5 5BG, UK

³ Heidelberger Institut für Theoretische Studien, Schloß-Wolfsbrunnengasse 35, 69118 Heidelberg, Germany

⁴ Astronomisches Rechen-Institut, Zentrum für Astronomie der Universität Heidelberg, Mönchhofstraße 12–14, 69120 Heidelberg, Germany

Accepted XXX. Received YYY; in original form ZZZ

ABSTRACT

We investigate the impact of strong initial magnetic fields in core-collapse supernovae of non-rotating progenitors by simulating the collapse and explosion of a $16.9 M_{\odot}$ star for a strong- and weak-field case assuming a twisted-torus field with initial central field strengths of $\approx 10^{12}$ G and $\approx 10^6$ G. The strong-field model has been set up with a view to the fossil-field scenario for magnetar formation and emulates a pre-collapse field configuration that may occur in massive stars formed by a merger. This model undergoes shock revival already 100 ms after bounce and reaches an explosion energy of 9.3×10^{50} erg at 310 ms, in contrast to a more delayed and less energetic explosion in the weak-field model. The strong magnetic fields help trigger a neutrino-driven explosion early on, which results in a rapid rise and saturation of the explosion energy. Dynamically, the strong initial field leads to a fast build-up of magnetic fields in the gain region to 40% of kinetic equipartition and also creates sizable pre-shock ram pressure perturbations that are known to be conducive to asymmetric shock expansion. For the strong-field model, we find an extrapolated neutron star kick of ≈ 350 km s⁻¹, a spin period of ≈ 70 ms, and no spin-kick alignment. The dipole field strength of the proto-neutron star is 2×10^{14} G by the end of the simulation with a declining trend. Surprisingly, the surface dipole field in the weak-field model is stronger, which argues against a straightforward connection between pre-collapse fields and the birth magnetic fields of neutron stars.

Key words: stars: massive – stars: magnetic fields – supernovae: general

1 INTRODUCTION

In the last few decades, there has been significant progress in our understanding of the role of magnetic fields in core-collapse supernovae. This is owed, in part, to rapid improvements in numerical modelling and computing capabilities.

Since traditional stellar evolution models (Heger et al. 2005) have predicted weak pre-collapse magnetic field strengths, most of the progress in understanding magnetic effects in core-collapse supernovae have been focused on the so-called magnetorotational mechanism (LeBlanc & Wilson 1970; Bisnovatyi-Kogan et al. 1976; Müller & Hillebrandt 1979; Burrows et al. 2007; Obergaulinger et al. 2009; Sawai et al. 2013; Masada et al. 2015; Mösta et al. 2015; Bugli et al. 2020; Obergaulinger & Aloy 2021). This mechanism relies on a rapidly differentially rotating star to amplify the weak magnetic fields, e.g., by the magnetorotational instability (MRI; Balbus & Hawley 1991; Akiyama et al. 2003) or an α - Ω -dynamo in the proto-neutron star (Duncan & Thompson 1992; Thompson & Duncan 1993; Raynaud et al. 2020). Strong magnetic stresses can then drive the explosion, usually in the form of collimated jets.

However, stellar evolution models also show magnetic braking causes the majority of supernova progenitor cores to rotate slowly

(Heger et al. 2005; Meynet et al. 2011) as the magnetic torques transport angular momentum to the envelope very efficiently. Even without magnetic braking, the winds of Galactic stars will prevent rapid rotation at core collapse. These predictions are bolstered by the white dwarf spin period distribution, which can only be explained if similarly efficient angular momentum transport mechanisms like magnetic torques operate in low-mass stars (Suijs et al. 2008). It is thus expected that the magnetorotational mechanism likely only operates in rare hyperenergetic supernovae explosions (known as “hypernovae”), which are sometimes linked to long-duration gamma-ray bursts (GRBs) as well (Woosley & Bloom 2006). These scenarios require special evolutionary pathways to limit the spin-down of the progenitor cores (e.g., Petrovic et al. 2005; Woosley & Heger 2006; Georgy et al. 2012, 2009; Cantiello et al. 2007; Aguilera-Dena et al. 2020).

The role of magnetic fields in supernovae outside the magnetorotational mechanism has so far received less attention. Without strong differential rotation, there is no obvious avenue for generating dynamically relevant fields that could become the main driver of an explosion. Nonetheless, some studies have explored the generation and impact of magnetic fields in non-rotating core-collapse supernovae in recent years. Early studies by Endeve et al. (2010, 2012) looked to understand the possible role of standing accretion shock instabilities (SASI) to amplify magnetic fields after core-collapse.

* E-mail: vishnu.rvejayan@monash.edu

† E-mail: bernhard.mueller@monash.edu

They found that while the SASI oscillations can amplify the magnetic fields on the neutron star to magnetar strengths, this does not affect global shock dynamics. Global studies in axisymmetric (2D) simulations by [Obergaullinger et al. \(2014\)](#), [Matsumoto et al. \(2020\)](#) and [Jardine et al. \(2022\)](#) with MHD and neutrino transport, find that even very strong magnetic fields ($\approx 10^{12}$ G), without rotation, only play an auxiliary in neutrino-driven explosions. However, recently, [Müller & Varma \(2020\)](#) have shown that in 3D, even very weak initial magnetic fields as low as 10^6 G can play a subsidiary role in aiding the neutrino-driven mechanism thanks to efficient amplification by a turbulent dynamo. A 3D study by [Matsumoto et al. \(2022\)](#) also showed that in more strongly magnetised models, the amplified magnetic field on large hot bubbles just behind a stalled shock can lead to a faster and more energetic explosion.

Another possibility for dynamically relevant magnetic fields, is that they might already be present in the progenitor. This is known as the fossil-field hypothesis for the generation of magnetic fields in neutron stars and, in particular, in magnetars. If the initial fields are strong enough, the compression via core-collapse alone would be sufficient to amplify the magnetic fields to magnetar strengths of 10^{14-15} G, through magnetic flux conservation ([Braithwaite & Spruit 2004](#); [Spruit 2009](#); [Ferrario et al. 2016](#)).

To explain magnetars by the fossil-field hypothesis, a remarkably strong field already would need to be present in the progenitor core in a subset of supernova progenitors. Based on a rough coincidence of the magnetar fraction and the fraction of roughly 7% of massive stars with unusually strong surface fields ([Donati & Landstreet 2009](#); [Grunhut et al. 2017](#); [Schöller et al. 2017](#)), a connection is often made between strongly magnetised massive stars on the main sequence and magnetars with the underlying assumption that the interior field is likewise strong and not destroyed through the subsequent evolutionary stages up to iron core collapse (see, e.g., [Quentin & Tout 2018](#), for the evolution of magnetised, low-mass stars up to white-dwarf formation). Connecting the origin of magnetar fields back to early evolutionary stages is appealing because stellar mergers might provide one natural avenue for producing a population of strongly magnetised stars roughly at the rate required to explain magnetars ([Schneider et al. 2019](#)); other channels for forming strongly magnetised OB stars are also conceivable (see, e.g., [Mestel 1999, 2001](#); [Moss 2001](#); [Donati & Landstreet 2009](#)), and this work should be viewed as being agnostic about the exact origin of the strong magnetic fields.

Rate arguments in favour of the fossil-field hypothesis are not uncontested, however. Some population synthesis models indicate that the simple fossil-field hypothesis based on the distribution of surface magnetic field strengths among massive stars cannot simultaneously reproduce both pulsar and magnetar populations ([Ferrario & Wickramasinghe 2006](#); [Makarenko et al. 2021](#)). It has also been found that the magnetar birth rate is comparable to that of neutron stars (and could be as high as the neutron star birth rate), which may leave too few known stars with surface $B > 10$ kG to account for the number of magnetars ([Woods 2008](#); [Keane & Kramer 2008](#)) and raises doubts whether fossil fields are the only means for generating magnetar-strength fields.

With many open questions about the origin of neutron star magnetic fields and recent theoretical results that suggest a broader role of magnetohydrodynamic effects in supernova explosions, further research into the impact of magnetic fields on supernova explosion dynamics and compact remnant birth properties is called for. In this study, we present new simulations of a strongly magnetised, non-rotating neutrino-driven supernova in 3D and compare this to a weakly magnetised model to better understand how the strength

of the magnetic field aids the explosion mechanism even without any initial rotation. While 1D stellar evolution models indicate only weak magnetic fields developing in supernova progenitors, our decision to explore the strongly magnetised regime is motivated by the fossil-field hypothesis and also by the 3D shell burning simulation of [Varma & Müller \(2021\)](#), which suggests the shell convection can generate rather strong magnetic fields of 10^{10-11} G in the oxygen shell.

Our paper is structured as follows: In Section 2, we describe the progenitor model as well as the initial conditions implemented in our simulations, this is followed by a description of the numerical methods of the code we used, CoCoNuT-FMT in Section 3. The results of the simulations are presented in Section 4 where we first look at the large-scale explosion dynamics, and analyse the role of the magnetic fields in the explosion, followed by an investigation of the resulting proto-neutron star (PNS) properties. We summarise our results and discuss their implications in Section 5.

2 PROGENITOR MODEL AND INITIAL CONDITIONS

We simulate the core collapse of a strongly magnetised, slowly-rotating massive star of $16.9 M_{\odot}$ that is the result of a binary merger of $8 M_{\odot}$ and $9 M_{\odot}$ stars as modelled in [Schneider et al. \(2019, 2020\)](#) in an attempt to reproduce the magnetic star τ Sco. The merger was simulated using the AREPO code, followed by 1D stellar evolution of the merger product in the MESA code. We map this MESA progenitor model to the CoCoNuT-FMT supernova code at the onset of core collapse when the maximum infall velocity has reached 1000 km s^{-1} . With a maximum angular velocity of $2.2 \times 10^{-8} \text{ rad s}^{-1}$ the rotation is, in fact, so slow that it can be neglected altogether, hence we do not map the angular velocity from the MESA progenitor model to CoCoNuT-FMT, and instead simulate the non-rotating case.

The MESA model is evolved until core collapse with the same setup as in [Schneider et al. \(2021\)](#). The entropy and density profiles mapped are shown in Figure 1.

Three-dimensional progenitor models of stars with strong fossil fields in the core are presently unavailable and unrealistic because they would require multi-dimensional stellar evolution calculations over secular time scales. We therefore manually specify a field configuration that is compatible with the expectations for a strong fossil field. Prior to mapping the merger progenitor into MESA, the magnetic field geometry of the star from [Schneider et al. \(2019\)](#) is 80–85% toroidal, but with a sizable poloidal component. This is consistent with the stable twisted-torus structure found in radiative zones found by [Braithwaite & Nordlund \(2006\)](#).

We hence initialise the magnetic field geometry using an analytical prescription from [Kamchatnov \(1982\)](#) for such twisted-torus fields. Although [Kamchatnov \(1982\)](#) did not prove the stability of this configuration, this is not essential for our purpose. The fields have no time to adjust before core collapse after the beginning of the simulation, and during the collapse even an initially stable magnetic field would become unstable anyway. The key point is that the configuration exhibits substantial magnetic helicity as one would expect from any realistic strong fossil field.

In spherical polar coordinates, the components A_r , A_{θ} , and A_{φ}

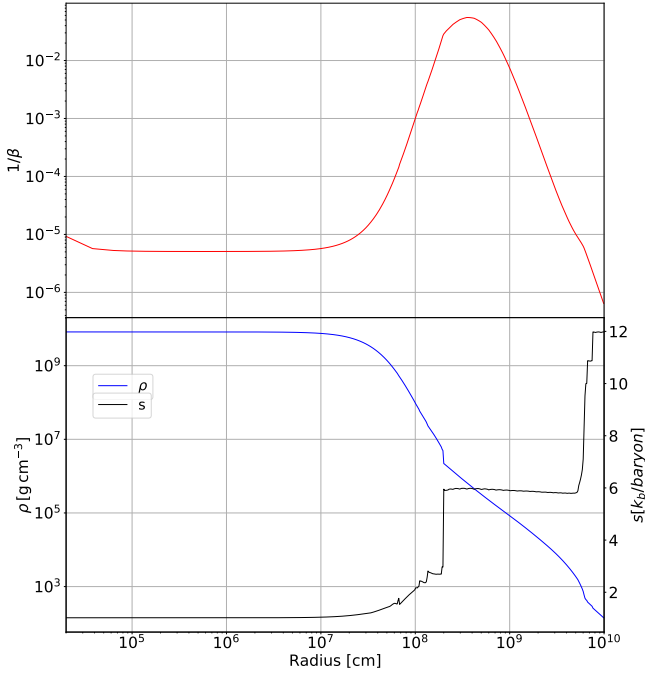


Figure 1. Inverse plasma- β at the onset of collapse for the strong-field model (top), and initial density and entropy profiles (bottom) for the progenitor.

of the vector potential for the initial field configuration are given by

$$A_r = B_0 \frac{(1 + \mathcal{R}^2) \cos \theta}{4(1 + 2\mathcal{R}^2 + \mathcal{R}^4)}, \quad (1)$$

$$A_\theta = B_0 \frac{(-1 + \mathcal{R}^2) \sin \theta}{4(1 + 2\mathcal{R}^2 + \mathcal{R}^4)}, \quad (2)$$

$$A_\phi = B_0 \frac{\mathcal{R} \sin \theta}{2(1 + 2\mathcal{R}^2 + \mathcal{R}^4)}, \quad (3)$$

where B_0 is the central (maximum) magnetic field strength, and $\mathcal{R} = r/R_0$ is a rescaled radial coordinate.

As we are investigating the role of magnetic fields in aiding the explosion mechanism for non-rotating supernova progenitors, we run two simulations using the same progenitor with different initial magnetic field strengths, namely a weak-field model, with $B_0 = 10^6$ G and a strong-field model with $B_0 = 10^{12}$ G and $R_0 = 5 \times 10^8$ cm.

The strong-field model serves as the representative case for the fossil-field magnetar progenitor scenario, whereas the weak-field model provides a control case. Since the magnetic field prescription from Equations (1–3) leads to a very sharp drop-off in magnetic field strength with radius, we scale the inner core to have magnetic field strengths of B_0 , such that for the strong magnetic field case, the pre-supernova oxygen shell has magnetic field strengths of $B = 10^{10} - 10^{11}$ G, (similar to Varma & Müller 2021). This is similar to the MESA progenitor model which should have a core field strength of $\gtrsim 10^{11}$ G, given magnetic flux is conserved from the original stellar merger calculation.

Without 3D progenitor models close to magnetohydrostatic equilibrium, a delicate balance must be struck in the choice of the initial field strength. The initial fields must not be too strong because this would render the initial pre-collapse structure highly inconsistent, but to realistically mimic a strong fossil field that would not have been overwhelmed by turbulent convective motions during the late burning stages, the magnetic stresses ought to be larger than the

expected turbulent Reynolds stresses from convection. The configuration chosen in this study places the ratio of magnetic to thermal pressure (inverse plasma- β) in the oxygen shell at 0.05 as a reasonable compromise (see Figure 1).

3 NUMERICAL METHODS

For our 3D simulations we employ the Newtonian magnetohydrodynamic (MHD) version of the CoCoNuT-FMT code as described in detail in Müller & Varma (2020); Varma & Müller (2021); Varma et al. (2021). The MHD equations are solved in spherical polar coordinates using the HLLC (Harten-Lax-van Leer-Contact) Riemann solver (Gurski 2001; Miyoshi & Kusano 2005) and piecewise parabolic reconstruction (Colella & Woodward 1984). The divergence-free condition $\nabla \cdot \mathbf{B} = 0$ is maintained using a modified version of the original hyperbolic divergence cleaning scheme of Dedner et al. (2002) and follows ideas of Tricco et al. (2016) to maintain energy conservation. Compared to the original cleaning method, we rescale the Lagrange multiplier ψ to $\hat{\psi} = \psi/c_h$, where c_h is the hyperbolic cleaning speed. Details of this approach and differences to Tricco et al. (2016) are discussed in the Appendix of Varma & Müller (2021). The extended system of MHD equations for the density ρ , velocity \mathbf{v} , magnetic field \mathbf{B} , the total energy density \hat{e} , mass fractions X_i , and the rescaled Lagrange multiplier $\hat{\psi}$ reads,

$$\partial_t \rho + \nabla \cdot \rho \mathbf{v} = 0, \quad (4)$$

$$\partial_t (\rho \mathbf{v}) + \nabla \cdot \left(\rho \mathbf{v} \mathbf{v} - \frac{\mathbf{B} \mathbf{B}}{4\pi} + P_t \mathcal{I} \right) = \rho \mathbf{g} - \frac{(\nabla \cdot \mathbf{B}) \mathbf{B}}{4\pi}, \quad (5)$$

$$\partial_t \hat{e} + \nabla \cdot \left[(e + P_t) \mathbf{v} - \frac{\mathbf{B}(\mathbf{v} \cdot \mathbf{B}) - c_h \hat{\psi} \mathbf{B}}{4\pi} \right] = \rho \mathbf{g} \cdot \mathbf{v} + \rho \dot{\epsilon}_{\text{nuc}}, \quad (6)$$

$$\partial_t \mathbf{B} + \nabla \cdot (\mathbf{v} \mathbf{B} - \mathbf{B} \mathbf{v}) + \nabla (c_h \hat{\psi}) = 0, \quad (7)$$

$$\partial_t \hat{\psi} + c_h \nabla \cdot \mathbf{B} = -\hat{\psi}/\tau, \quad (8)$$

$$\partial_t (\rho X_i) + \nabla \cdot (\rho X_i \mathbf{v}) = \rho \dot{X}_i, \quad (9)$$

where \mathbf{g} is the gravitational acceleration, P_t is the total pressure, \mathcal{I} is the Kronecker tensor, τ is the damping timescale for divergence cleaning, and $\dot{\epsilon}_{\text{nuc}}$ and \dot{X}_i are energy and mass fraction source terms from nuclear reactions. This system conserves the volume integral of a modified total energy density \hat{e} , which also contains the cleaning field $\hat{\psi}$,

$$\hat{e} = \rho \left(\epsilon + \frac{v^2}{2} \right) + \frac{B^2 + \hat{\psi}^2}{8\pi}, \quad (10)$$

where ϵ is the mass-specific internal energy.

To reduce numerical dissipation near the grid axis in our simulations, we have modified the mesh coarsening algorithm of Müller et al. (2019a) by implementing a third-order accurate slope-limited prolongation scheme. Neutrinos are treated using the FMT (fast multi-group transport) scheme of Müller & Janka (2015a), which solves the energy-dependent zeroth moment equation for three neutrino species in the stationary approximation using a closure obtained from a two-stream solution of the Boltzmann equation

The two models are run with a grid resolution of $550 \times 128 \times 256$ zones in r , θ and φ (corresponding to 1.4° in angle), an exponential grid in energy spaces with 21 zones from 4 MeV to 240 MeV. The simulations use the equation of state of Lattimer & Swesty (1991) with an incompressibility modulus of $K = 220$ MeV at high densities, and an ideal gas consisting of photons, electrons, positrons, and non-relativistic nucleons and nuclei, in conjunction with an NSE solver above 5 GK and a flashing treatment at lower temperatures (Rampp & Janka 2000).

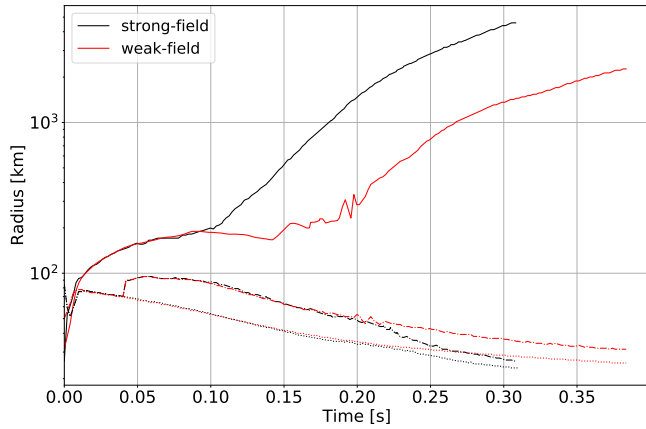


Figure 2. Evolution of the maximum shock radius (solid), PNS radius (dotted), and gain radius (dash-dotted) for the strong-field (black) and weak-field (red) models.

4 RESULTS

4.1 Explosion Dynamics

Both the strong- and weak-field models collapse to a PNS within the same time, ≈ 0.1 s after the models are mapped to 3D. In Figure 2, we see that while their initial shock trajectories are very similar, they begin to deviate significantly after about 0.1 s post-bounce, at which point the strong magnetic field model undergoes much more rapid shock expansion. In the weak-field case, the shock is also revived, but shock expansion sets in about 0.05–0.1 s later. Up to the time of explosion in the strong-field model, the mass accretion rate agrees perfectly in both runs (Figure 3), indicating that the strong initial field does not spuriously affect the *spherically-averaged* collapse dynamics. After the onset of the explosion, the accretion rate drops visibly in both cases. In the strong-field model, net accretion on the PNS (defined as the radius where the angle-averaged density reaches 10^{11} g cm $^{-3}$) ceases shortly after 0.2 s post-bounce. The subsiding accretion is responsible for a change in PNS surface structure that is reflected in the evolution of the PNS radius and the gain radius in Figure 2. While the two models match very closely in terms of PNS radius and gain radius for the first 0.225 s, they then start to diverge, with the PNS radius and gain radius of the strong magnetic field models dropping more rapidly.

Shock revival also has consequences for the neutrino luminosities and mean energies, which are shown in Figure 4. Up until 0.1 s after bounce, the neutrino-emission is very similar in both models. Small differences arise because of stochastic variation in the early post-bounce entropy profiles that are imprinted on the PNS by prompt convection and slightly change the thermodynamics conditions at the neutrinosphere (cp. Müller & Varma 2020). Once the shock starts to expand in the strong-field model, the electron neutrino and antineutrino luminosities drop significantly faster than in the weak-field model, and the rise of their mean energies is slower. Interestingly, the heavy-flavour neutrino mean energy remains higher in the strong-field model, which is consistent with faster contraction of the PNS. It is also noteworthy that there are small differences in the neutrino emission between the strong- and weak-field models prior to shock revival, which would actually suggest slightly better heating conditions in the weak-field model. These can be ascribed to minute differences in the collapse phase and the PNS structure at early post-bounce times that ultimately stem from the slight perturbation of the spherical collapse dynamics by the introduction of the initial fields.

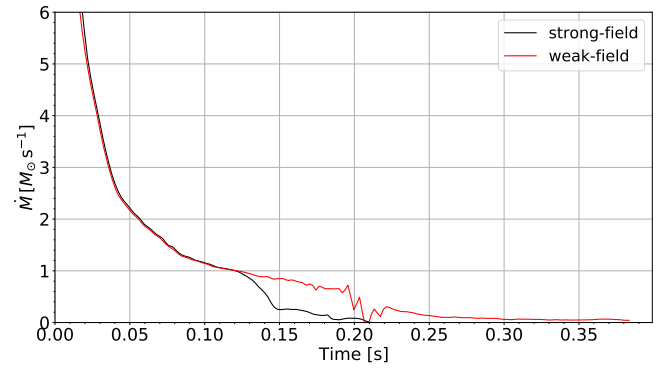


Figure 3. Mass accretion rate \dot{M} for the strong-field model (black) and for the weak-field model (red), calculated at a radius of 250 km.

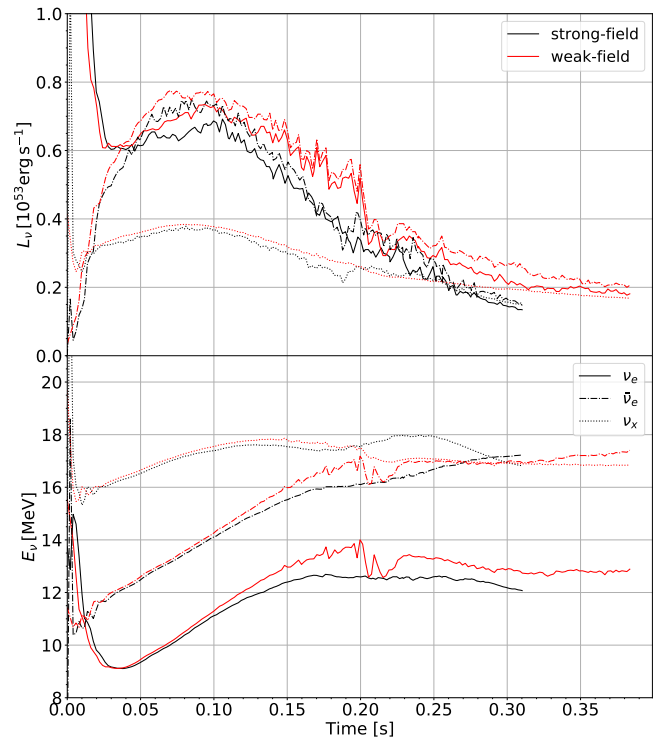


Figure 4. Neutrino luminosities (top) and mean energies (bottom) of electron neutrinos (ν_e), electron antineutrinos ($\bar{\nu}_e$) and heavy-flavour neutrinos (ν_x), measured at a radius of 2000 km.

Figure 5 shows the diagnostic explosion energy E_{expl} (Buras et al. 2006) for both models. The diagnostic explosion energy is defined as an integral over the region that is nominally unbound,

$$E_{\text{expl}} = \int_{e_{\text{tot}} > 0} \rho e_{\text{tot}} dV, \quad (11)$$

where e_{tot} is the total energy density, i.e., the sum of the internal, kinetic, gravitational, and magnetic energy density.

The diagnostic explosion energy of the strong-field model begins to rise around the time when the shock trajectories of the two models deviate, and reaches more than 9×10^{50} erg by the end of the simulation. The explosion energy already appears to level off at this stage, which is rather unusual when compared to current 3D hydrodynamic simulations of core-collapse supernova explosions. Long-term 3D

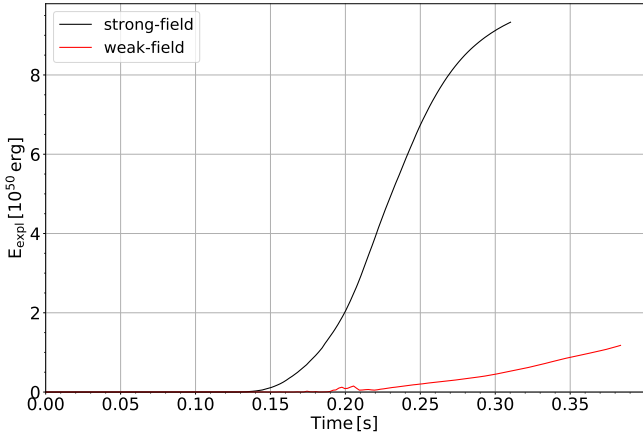


Figure 5. Evolution of the diagnostic explosion energy E_{expl} for the strong-field model (black) and the weak-field model (red).

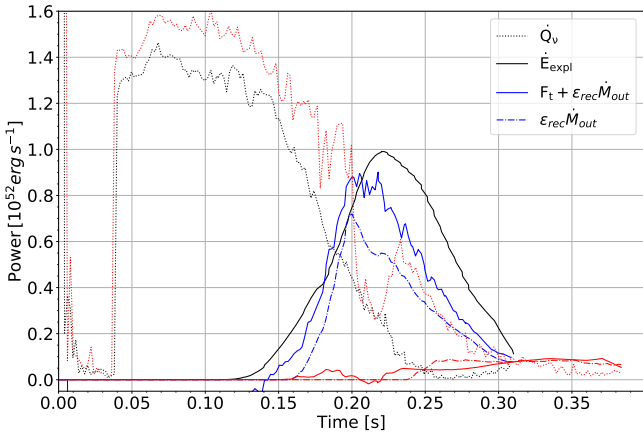


Figure 6. Comparison of the growth rate \dot{E}_{expl} of the diagnostic explosion energy (solid black and red curves) to the approximation for the rate of energy ejection into the ejecta from Equation (13) (solid blue curve), which accounts for the release of $\epsilon_{\text{rec}} = 6$ MeV/baryon by nucleon recombination for the measured mass outflow rate \dot{M}_{out} and the measured magnetohydrodynamic energy flux F_t at the base of the gain region of the strongly magnetised model (blue). The nuclear recombination power $\epsilon_{\text{rec}}\dot{M}_{\text{out}}$ is also plotted on its own for both models (dash-dotted blue and red curves). The volume-integrated neutrino heating rate \dot{Q}_ν is also shown (dotted curves).

explosion models of massive progenitors typically show a sustained rise of the explosion energy over up to several seconds (Müller 2015; Bruenn et al. 2016; Bollig et al. 2021), but at a significantly smaller growth rate, more reminiscent of the weak-field model, which has only reached about 10^{50} erg. The unusually rapid growth and saturation of the explosion energy is further emphasised by Figure 6, which shows that the rate of growth dE_{expl}/dt peaks at 10^{52} erg s^{-1} about 0.22 s post-bounce, and drops by more than a factor of five afterwards.

Strong initial fields thus evidently have a major impact on the explosion dynamics, allowing the model to reach a typical supernova explosion energy (Kasen & Woosley 2009; Murphy et al. 2019) within only 0.3 s after bounce. As we shall show, this effect is largely of an indirect nature. It comes about because the strong initial fields help trigger the explosion early, rather than from direct delivery of the explosion energy by magnetic stresses as in the magnetorotational paradigm. The explosion is energised in a similar manner as in

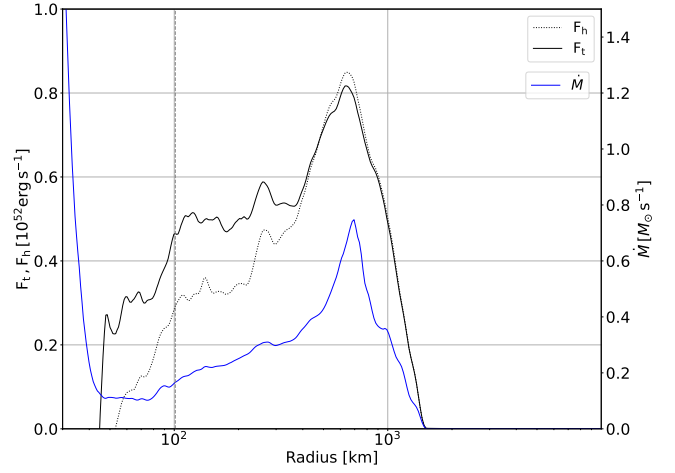


Figure 7. Radial profiles of the total magnetohydrodynamic energy flux F_t with rest masses subtracted (black, solid), the purely hydrodynamic total enthalpy flux F_h (black, dotted), and the mass outflow rate \dot{M}_{out} (blue) for the strong-field model at 0.20 s post-bounce. The energy and mass fluxes are computed as integrals over the area covered by outflows with $v_r > 0$. The vertical dashed line at ≈ 100 km indicates where does the angle-averaged total energy in the outflows become positive.

existing hydrodynamics models of neutrino-driven explosions with a few subtle differences related to early shock revival.

Previous studies by Marek et al. (2006); Müller (2015); Bruenn et al. (2016) have shown that for the neutrino-driven explosion mechanism, the growth of the diagnostic explosion energy is largely determined by the mass outflow rate, \dot{M}_{out} of the ejecta, which are first lifted to $e_{\text{tot}} \approx 0$ by neutrino heating, before obtaining most of their net positive energy from nucleon recombination. Ignoring secondary effects like the scooping-up of bound material by the shock and losses of explosion energy by turbulent braking of the expanding neutrino-heated bubbles, this results in a growth rate of the explosion energy of $\dot{E}_{\text{expl}} \approx \epsilon_{\text{rec}}\dot{M}_{\text{out}}$, where ϵ_{rec} is the recombination energy per unit mass.

Comparing the rate of energy release $\epsilon_{\text{rec}}\dot{M}_{\text{out}}$ by nucleon recombination to the rate of growth of the explosion energy is rather tricky for the strong-field model since \dot{M}_{out} is non-stationary and varies strongly with radius (Figure 7), unlike in models with later shock revival where $\dot{M}_{\text{out}} \approx \text{const.}$ over a large range in radius (see, e.g., Figure 18 of Müller 2015). To capture the energy release by nuclear recombination with reasonable accuracy during a rather non-stationary outflow, it is critical to evaluate \dot{M}_{out} not too far away from the actual recombination radius. In our subsequent analysis, we evaluate \dot{M}_{out} at a radius of 400 km by integrating over all directions where the radial velocity component v_r is positive,

$$\dot{M}_{\text{out}} = \int_{v_r > 0} \rho v_r r^2 d\Omega. \quad (12)$$

Even in this case, however, nucleon recombination can only account for a little more than half of the growth rate of the explosion energy.

The extra energy input into the explosion can be explained by $P dV$ work (and to some extent, work by magnetic stresses) by the underlying layers on the ejecta region. It is noteworthy that a more significant role of the magnetohydrodynamic energy flux into the ejecta region compared to recombination was also found for early explosions in axisymmetry (Bruenn et al. 2016) and for some mass shells in rapidly developing electron-capture supernova explosions (Janka et al. 2008).

Taking into account the hydrodynamic energy flux into the ejecta region we expect the explosion energy to grow as

$$\frac{dE_{\text{expl}}}{dt} \approx F_t + \epsilon_{\text{rec}} \dot{M}_{\text{out}}, \quad (13)$$

where F_t is the total magnetohydrodynamic energy flux,

$$F_t = \int_{v_r > 0} r^2 \left[(\rho e + P_t + \rho \Phi) v_r + \frac{\mathbf{B}(\mathbf{v} \cdot \mathbf{B})}{4\pi} \right] d\Omega. \quad (14)$$

In Figure 6, we compare $F_t + \epsilon_{\text{rec}} \dot{M}_{\text{out}}$ to \dot{E}_{expl} using a value of $\epsilon_{\text{rec}} = 6 \text{ MeV}/m_b$ (where m_b is the atomic mass unit), which accounts for incomplete recombination as well as some turbulent mixing. The growth of E_{expl} is described reasonably well by the assumption of delivery by nuclear recombination and an additional, subdominant contribution by $P dV$ -work and magnetic stresses, although $\epsilon_{\text{rec}} \dot{M}_{\text{out}}$ alone somewhat underestimates the actual growth rate.

To quantify the direct role of magnetic fields in powering the explosion, we also compare the total magnetohydrodynamic energy flux F_t to the purely hydrodynamic total enthalpy flux F_h ,

$$F_h = \int_{v_r > 0} r^2 (\rho e + P + \rho \Phi) v_r d\Omega, \quad (15)$$

where the magnetic pressure and magnetic stresses are excluded and only the gas pressure P enters aside from purely advective terms. At the base of the ejecta region at 100 km (where the angle-averaged total energy in the outflows becomes positive), the hydrodynamic enthalpy flux F_h accounts for most of the total energy flux F_t into the ejecta. The rest of the energy flux into the ejecta is due to work by magnetic pressure and magnetic stresses. Their contribution is non-negligible, but smaller than the hydrodynamics flux F_h at the base of the ejecta region.

The rate of growth of the explosion energy is therefore well explained by nuclear recombination and some additional magnetohydrodynamic energy flux into the ejecta region. The unusually rapid growth of the explosion energy is merely the result of a rather high mass outflow rate, and this in turn is simply due to the early onset of the explosion at a time when the mass accretion rate is still high (close to $1 M_{\odot} \text{ s}^{-1}$) and the mass of the gain region is large. At first glance, the fact that \dot{E}_{expl} even exceeds the volume-integrated neutrino heating rate \dot{Q}_{ν} in the gain region (Figure 6) might suggest that additional powering other than neutrino heating is needed to explain the high mass outflow rate. For a steady-state outflow one would expect a ratio $\dot{E}_{\text{expl}}/\dot{Q}_{\nu} \approx \epsilon_{\text{nuc}}/|e_{\text{bind}}|$, where $|e_{\text{bind}}|$ is the typical binding energy of neutrino-heated matter before it turns away from the PNS to be ejected, and if $|e_{\text{bind}}|$ is taken as the net binding energy at the gain radius, one usually obtains $\dot{E}_{\text{expl}}/\dot{Q}_{\nu} < 1$. The rather small magnetohydrodynamic energy flux of only $\sim 3 \times 10^{51} \text{ erg s}^{-1}$ deeper in the gain region at radii of less than 100 km in Figure 7 argues against an additional power source for lifting the ejecta to roughly zero net energy before recombination. The large ratio $\dot{E}_{\text{expl}}/\dot{Q}_{\nu}$ is instead explained by other effects. First, Müller et al. (2017) pointed out that the effective turnaround radius of the ejecta can become quite large in a developing explosion, so that material need not be lifted out of the potential well all the way from the gain radius. Second, the average binding energy in the gain region decreases quite quickly in the strong-field model as shown in Figure 10. Third, for a non-stationary outflow, \dot{E}_{expl} and \dot{Q}_{ν} cannot be compared at the same time because there is a delay between peak neutrino heating of an ejected mass element in the gain region and the time when it acquires contributes to the explosion energy after undergoing recombination.

The dynamics of the outflows in the strong-field model thus clearly

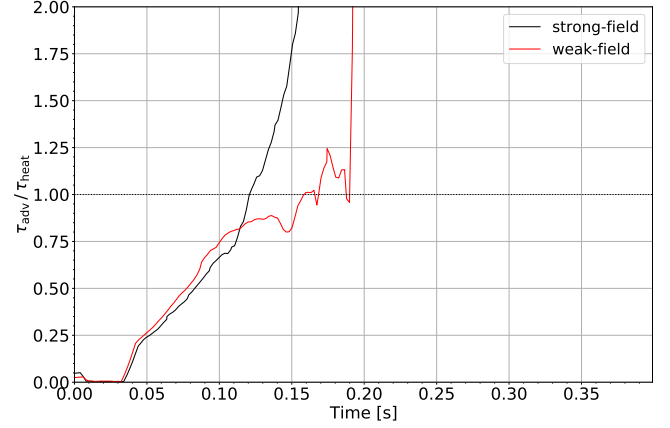


Figure 8. Ratio of the advection timescale τ_{adv} to the heating timescale τ_{heat} in the gain region of the strong-field model (black) and the weak-field model (red). A horizontal dotted line indicates the threshold criterion $\tau_{\text{adv}}/\tau_{\text{heat}} = 1$ for runaway shock expansion in the neutrino-driven mechanism.

point towards an *indirect* effect of the initial field on the explosion energy. The key role of the magnetic fields is to *trigger* shock revival early, which provides the conditions for a rapid growth of the explosion energy. We therefore need to elucidate how the strong initial fields precipitate shock revival.

4.2 Dynamics of the Gain Region and Evolution Towards Shock Revival

Contrary to the explosion energetics, the strong initial magnetic fields play a clearly recognisable role in the dynamics of the gain region prior to and around shock revival. The earlier onset of explosion in the strong-field model appears to be partly due to similar effects as in Müller & Varma (2020), where the magnetic fields in the gain region were generated by a turbulent dynamo, but our analysis also reveals a new phenomenon that is peculiar to stellar cores with strong pre-collapse fields.

To analyse the dynamics of the gain region, we first consider the critical ratio of the advection and heating time scales $\tau_{\text{adv}}/\tau_{\text{heat}}$, (Figure 8), which quantifies the conditions for runaway shock expansion by neutrinos (Buras et al. 2006). The advection and heating timescale τ_{adv} and τ_{heat} are defined as

$$\tau_{\text{adv}} = \frac{M_g}{\dot{M}}, \quad (16)$$

$$\tau_{\text{heat}} = \frac{|E_g|}{\dot{Q}_{\nu}}, \quad (17)$$

where E_g and M_g are the binding energy and mass of the gain region, \dot{M} is the mass accretion rate, and \dot{Q}_{ν} is the volume-integrated neutrino heating rate.

It is noteworthy that by the time the shock starts to expand in the strong-field model and deviates from the shock trajectory in the weak-field model at 0.1 s after bounce, $\tau_{\text{adv}}/\tau_{\text{heat}}$ still has not reached the critical threshold $\tau_{\text{adv}}/\tau_{\text{heat}} \approx 1$ and is actually slightly *lower* than in the weak-field model. The lower ratio $\tau_{\text{adv}}/\tau_{\text{heat}}$ can be explained by the slightly lower neutrino heating rates in the strong-field model (Figure 6; cp. the discussion of the neutrino luminosities in Section 4.1). While $\tau_{\text{adv}}/\tau_{\text{heat}} \approx 1$ is reached in the strong-field model about 0.02 s later, this provides strong evidence that dynamical effects of magnetic fields initially aid shock expansion (even though

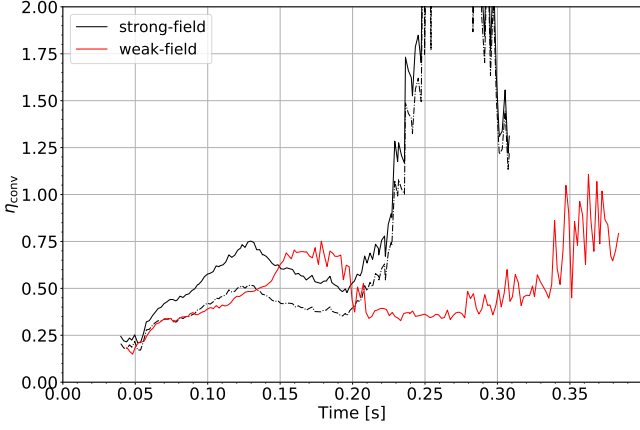


Figure 9. Evolution of the convective efficiency η_{conv} in the gain region as defined by Equation (18). The solid lines show the convective efficiency based on the total kinetic and magnetic turbulent energy $E_{\text{kin}} + E_{\text{mag}}$, while only the turbulent kinetic energy E_{kin} is included for dash-dotted lines. Black and red curves are used for the strong- and weak-field model, respectively. Only the solid line is visible for the weak-field model because the magnetic energy in the gain region is negligible.

their importance as a subsidiary driver of the explosion diminishes once the runaway criterion is met).

We evidence for important dynamical effects of the strong seed fields both inside the gain region (as in Müller & Varma 2020) and outside the shock. Their impact inside the gain region can be gauged by the convective efficiency parameter for the conversion of neutrino heating to turbulent kinetic and magnetic energy in the gain region, (Müller & Janka 2015b; Müller & Varma 2020),

$$\eta_{\text{conv}} = \frac{(E_{\text{kin}} + E_{\text{B}})/M_{\text{gain}}}{[(r_{\text{sh}} - r_{\text{gain}})\dot{Q}_{\nu}/M_{\text{gain}}]^{2/3}}, \quad (18)$$

As shown by Figure 9, η_{conv} is $\lesssim 50\%$ higher than in the weak-field model until about 0.125 s post-bounce. The convective efficiency computed from the turbulent kinetic energy alone roughly equals the total convective efficiency in the weak-field model, in which the turbulent magnetic energy is negligible during this phase. The situation is thus analogous to that in Müller & Varma (2020); the turbulent magnetic energy is filled as an extra energy reservoir on top of the kinetic turbulent energy, which is fed by the neutrino heating. Different from Müller & Varma (2020), the increase in convective efficiency is observed as soon as convection develops in the strong-field model, however.

The early boost to the convective efficiency is due to the strong seed fields, which allow the magnetic fields in the gain region to reach levels close to equipartition with little amplification, compared to the situation with weak seed fields, where this takes an appreciable amount of time despite exponential amplification by a turbulent dynamo (Müller & Varma 2020). This is illustrated by Figure 11, which shows the turbulent kinetic energy E_{kin} and the magnetic field energy E_{B} in the gain region. E_{kin} and E_{B} are computed as

$$E_{\text{kin}} = \int \frac{1}{2} \rho |\mathbf{v}'|^2 dV, \quad (19)$$

$$E_{\text{B}} = \int \frac{|\mathbf{B}|^2}{8\pi} dV, \quad (20)$$

where \mathbf{v}' denotes the fluctuations of the velocity around its spherical Favre average (i.e. $\mathbf{v}' = \mathbf{v} - \langle \mathbf{v} \rangle$). We also show the ratio $E_{\text{B}}/E_{\text{kin}}$ of the magnetic and kinetic turbulent energy, in Figure 12. The strong

initial magnetic field strength model undergoes a very brief exponential magnetic field amplification process, placing the ratio of $E_{\text{B}}/E_{\text{kin}} \approx 40\%$ when runaway expansion occurs, similar to the saturation value found in Müller & Varma (2020). By contrast, although the weak magnetic field model undergoes a rapid magnetic field amplification process in the gain region after ≈ 0.20 s, the neutrino-driven mechanism launches the shock before the magnetic energies are strong enough to affect the dynamics of the gain region. We note that there is rough energy equipartition between the radial magnetic fields (generated predominantly by radial stretching of field lines) and the non-radial components (generated predominantly by non-radial shear flows). The energies $E_{\text{B},r}$ and $E_{\text{B},\theta\phi}$ in the radial and non-radial components,

$$E_{\text{B},r} = \int \frac{B_r^2}{8\pi} dV, \quad (21)$$

$$E_{\text{B},\theta\phi} = \int \frac{B_\theta^2 + B_\phi^2}{8\pi} dV, \quad (22)$$

are shown in Figure 12, as a ratio with the kinetic energy in the gain region. For approximate equipartition, the dynamical effect of magnetic fields on shock propagation through tension and pressure forces is arguably quite neutral, but storing extra energy in magnetic fields will still make it easier to unbind material and release additional energy back into the neutrino-heated material as it expands. The detailed dynamical impact of the magnetic fields on the quasi-hydrostatic structure of the gain region still remains to be investigated more rigorously; we recall that the chain of effects through which turbulence facilitates shock expansion is highly non-trivial even in the hydrodynamics case (e.g., Mabanta & Murphy 2018).

In summary, a similar mechanism operates in the strong-field model as in the MHD-aided explosion of Müller & Varma (2020); magnetic fields in the gain region become sufficiently strong to boost the overall turbulent energy in the gain region and thereby aid shock revival. The key difference is that this process occurs significantly earlier due to the strong seed fields. As in Müller & Varma (2020), it is not possible to disentangle precisely which turbulent terms (e.g., the magnetic stresses in the momentum equation, the flux terms in the energy equation, etc.) in the MHD equations are responsible for precipitating shock expansion. Based on the ratio $E_{\text{B}}/E_{\text{kin}}$, the magnetic stress terms are clearly non-negligible. There is somewhat better evidence than in Müller & Varma (2020) that magnetic fields also palpably reduce the binding energy of the gain region (Figure 10). E_{bind} in the strong-field models starts to visibly deviate from the weak-field model from ≈ 0.09 s after bounce, i.e. already slightly before the shock trajectories diverge.

In addition to increasing the turbulent in the gain region by jump-starting turbulent field amplification, the strong initial fields affect the dynamics by modifying the pre-shock conditions, similar to what occurs for “perturbation-aided explosions” in progenitors with vigorous convection in the oxygen or silicon shell (Couch et al. 2015; Müller & Janka 2015b; Müller et al. 2017). In the perturbation-aided mechanism, vortical convective motions are translated to sizable perturbations of the pre-shock density and ram pressure by advective-acoustic coupling (Müller & Janka 2015b; Abdikamalov & Foglizzo 2020; Abdikamalov et al. 2021), which then facilitate asymmetric shock expansion. We demonstrate that the initial fields assumed in our models also lead to differential infall and large-scale asymmetries in the pre-shock ram pressure. To this end, we consider the relative ram pressure perturbations P'_{ram} ,

$$P'_{\text{ram}} = \frac{P_{\text{ram}} - \langle P_{\text{ram}} \rangle}{\langle P_{\text{ram}} \rangle}, \quad (23)$$

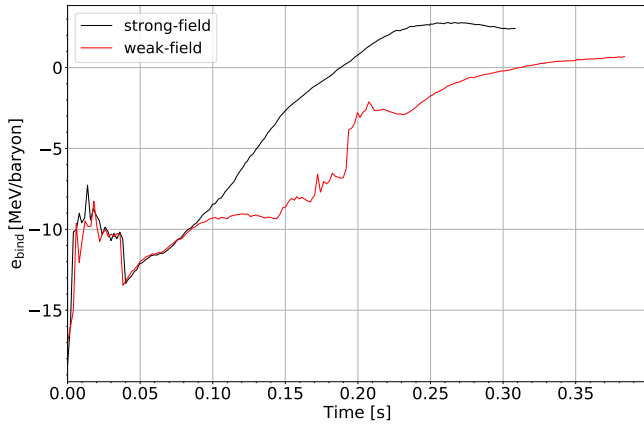


Figure 10. Average specific binding energy e_{bind} in the entire gain region of the strong-field model (black) and the weak-field model (red).

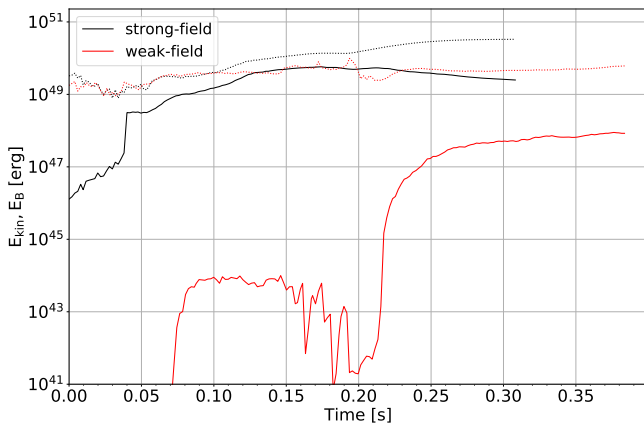


Figure 11. Evolution of the total magnetic (solid) and turbulent kinetic (dotted) energy within the gain region (Equations 19 and 20) for the strong-field model (black) and the weak-field model (red).

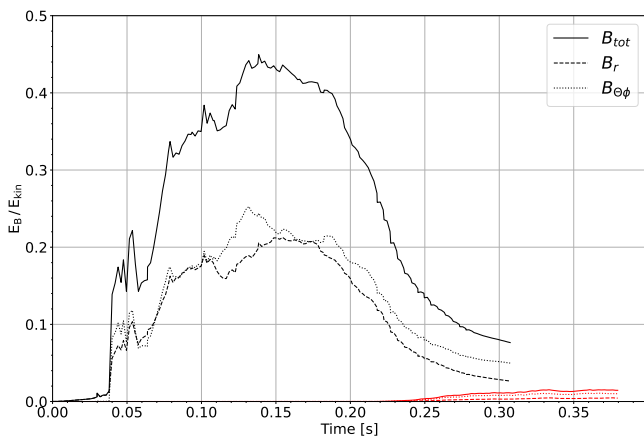


Figure 12. Evolution of the ratio between the total magnetic and turbulent kinetic energy within the gain region for strong-field model (black) and the weak-field model (red). For both models, the ratio is plotted for the total magnetic energy (solid), the radial only component (dashed), and the angular components (dotted) of the magnetic energy.

where $P_{\text{ram}} = \rho v_r^2$ is the angle-dependent ram pressure, and $\langle P_{\text{ram}} \rangle$ is its average over solid angle. We evaluate P'_{ram} at a radius of 200 km, which is small enough to capture the pre-shock conditions sufficiently well but larger than the maximum shock radius before shock revival. 2D Hammer projection of the ram pressure perturbations at this radius are shown for the strong- and weak-field models at different times in Figure 13. In the strong-field model, large-scale asymmetries in the pre-shock ram pressure clearly emerge already at 0.05 s and grow considerably stronger shortly before shock revival at 0.09 s. The contrast between the directions of high and low ram pressure reaches about 20%, and there is a clear large-scale asymmetry with a ram pressure deficit in the Southern hemisphere, an excess at mid-latitudes in the Northern hemisphere, and a deficit in a smaller region above latitudes of $\gtrsim 60^\circ$ in the Northern hemisphere. Such large-scale perturbations are most conducive to perturbation-aided shock revival (Müller & Janka 2015b). The large-scale component of the perturbations is in fact more clearly visible than in simulations based on 3D progenitor models with oxygen shell convection (cp. Figure 8 in Müller et al. 2017), while the magnitude of relative pressure perturbation are of a similar magnitude. In the weak-field model, the magnetic fields are not strong enough to dynamically affect the infall. Weaker pre-shock ram pressure perturbations emerge from numerical noise in the infall region in this case. These become weaker in time, and are dominated by small-scale structures. Figure 14 shows a spherical harmonics decomposition of P'_{ram} to illustrate the different magnitude and scale of the ram pressure perturbations in the two models more quantitatively. We compute the spectrum $\hat{P}_{\text{ram},\ell}$ as

$$\hat{P}_{\text{ram},\ell} = \sqrt{\sum_{m=-\ell}^{\ell} \left| \int Y_{\ell m}^* P'_{\text{ram}} d\Omega \right|^2}. \quad (24)$$

The spherical harmonic functions are orthonormalised and calculated using the SHTOOLS package (Wieczorek et al. 2016). The presence of a dipole and quadrupole of growing amplitude in the strong-field model is clearly visible in Figure 14. The precise relation of the pre-shock ram pressure perturbations to the initial magnetic field structure is not yet fully transparent, and needs to be investigated further using linear perturbation theory in future (see discussion below). In particular, the emergence of an appreciable North-South asymmetry, which could be related to an instability of the initial twisted-torus field configuration, warrants further attention.

As shown by Figure 15, the forcing by asymmetries in ram pressure is reflected in the explosion geometry of the strong-field model. The most prominent high-entropy plume aligns with the region of lower ram pressure in the Southern hemisphere. There is a somewhat weaker neutrino-heated plume around the North polar axis as well, corresponding to the ram pressure deficit above latitudes of 60° in the bottom left panel of Figure 13. The prominent downflows at moderate latitudes in the Northern hemisphere are aligned with the regions of excess ram pressure. In the weakly magnetised model, the explosion geometry is characterised by a big plume along the North polar axis and several less prominent plumes. In this case, the emergence of a prominent polar plume is likely facilitated by the grid geometry; a tendency towards grid-aligned explosion in weakly perturbed models has been observed before with the CoCoNuT code, though it is not universal (see, e.g., model he3.5 in Müller et al. 2019b). There is no clear relation to the pre-shock ram pressure perturbations.

It should be noted, however, that the mechanism whereby magnetic fields are converted to acoustic perturbations during collapse still needs to be investigated in future work along the lines of existing linear theory for the amplification of hydrodynamic perturbations (Lai & Goldreich 2000; Takahashi & Yamada 2014; Abdikamalov

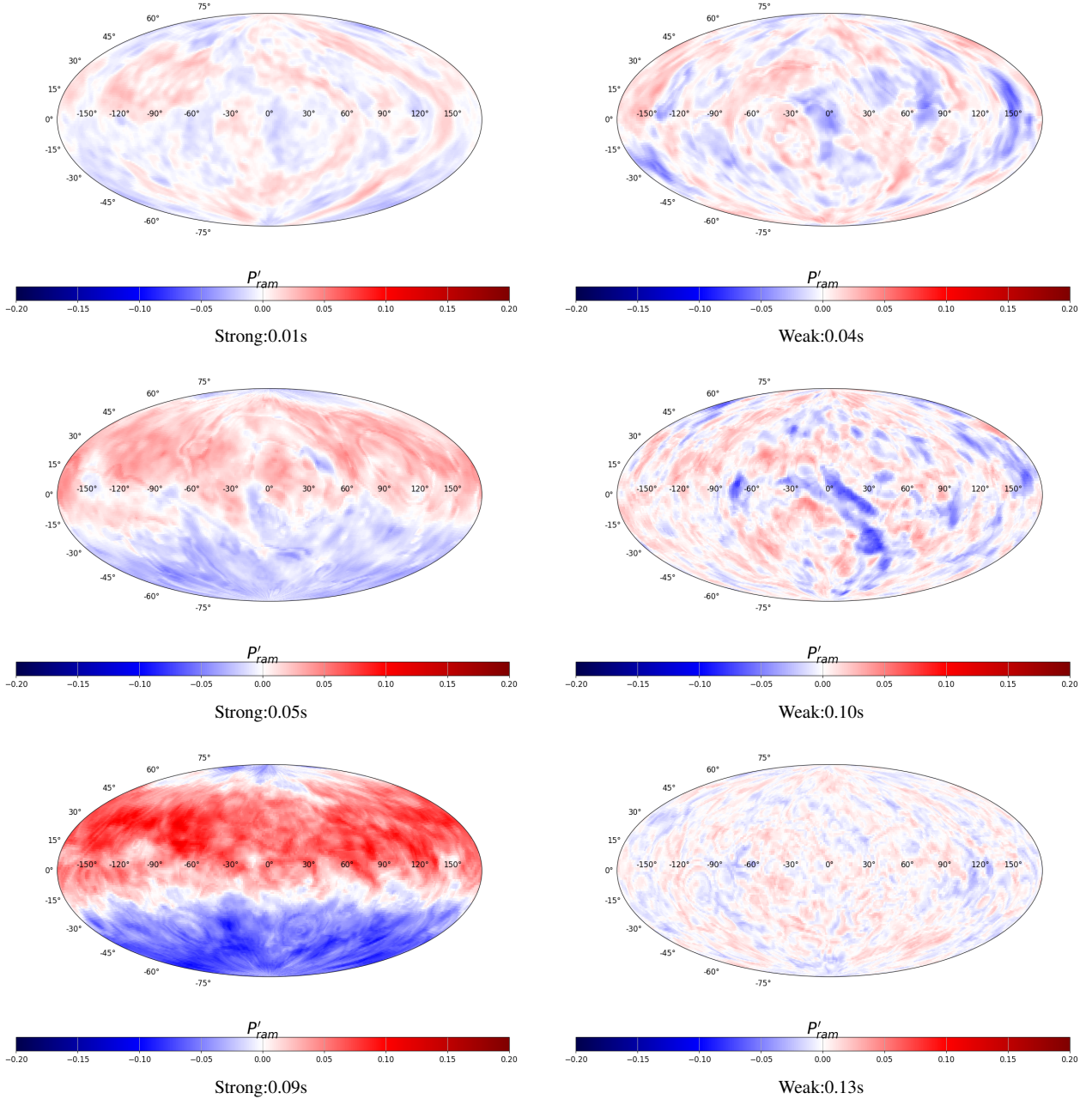


Figure 13. Relative ram pressure perturbations P' ahead of the shock for the strong-field model (left column) and the weak-field model (right column) at a radius of 200 km at different times (denoted below each panel). The final row shows the ram pressure perturbations amplitudes immediately before the maximum shock radius reaches 200 km.

& Fogliizzo 2020; Abdikamalov et al. 2021). The nature of the magnetohydrodynamic perturbations in the progenitor warrants further scrutiny. In the magnetohydrodynamic case, the linear evolution during collapse can be expected to be richer with interactions between different waves families beyond the mechanism of vortical-acoustic and entropic-acoustic coupling in the hydrodynamic case.

There is also the question whether the twisted-torus initial conditions adequately approximate the magnetic field structure in the progenitor. For the hydrodynamic case, it is important to take into account that the initial perturbation spectrum from weakly compressible convective flow is dominated by vorticity and entropy perturbations and not by acoustic perturbations (Müller & Janka 2015b;

Abdikamalov & Fogliizzo 2020). In the absence of consistent 3D progenitor models, this can adequately be captured by imposing a solenoidal flow geometry in convective regions in the progenitor. In the fossil-field scenario, it is less clear whether imposing a reasonable twisted-torus field geometry already captures the relevant physical constraints on the wave structure of the pre-collapse perturbations. This is particularly important for the strong-field case, where the magnetic fields are strong enough to noticeably perturb hydrostatic equilibrium with initial values of a few 10^{-2} for the ratio of magnetic to thermal pressure in the oxygen shell. For this reason, MHD models of quasi-equilibria with strong fossil fields in supernova progenitors are an important desideratum for the future.

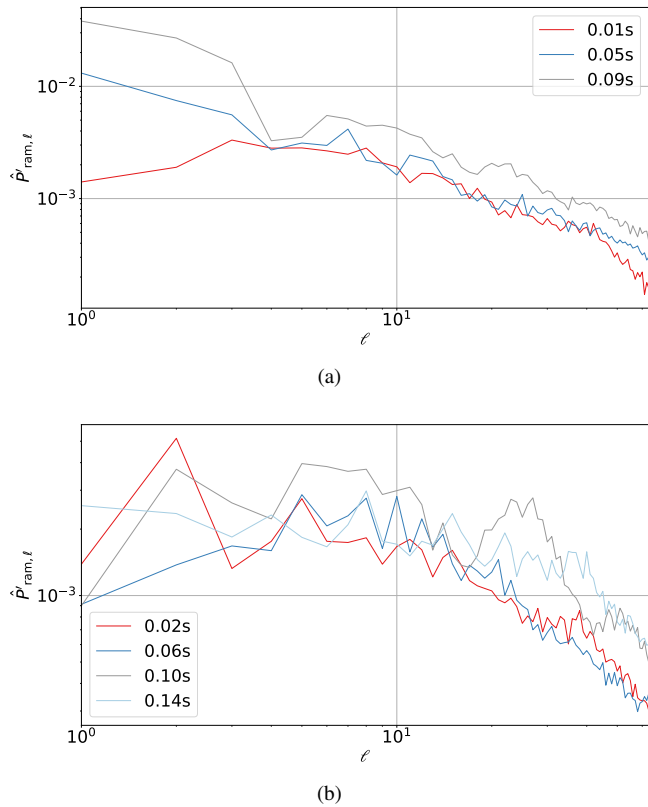


Figure 14. Spectrum $\hat{P}'_{\text{ram},\ell}$ of the ram pressure perturbations (Equation 24) at 200 km, ahead of the shock, (a) for the strong-field model and (b) for the weak-field model.

4.3 Neutron Star Properties

We next consider the birth properties of the neutron star produced in the two simulation. These are particularly relevant for evaluating the prospects for the fossil-field scenario for magnetar formation, although it must be borne in mind that the magnetic field and spin rate of the neutron star can still be affected by processes that occur on longer time scales than we can simulate here, such as spin-up and field burial due to fallback.

We show the bulk properties of the PNS in Figure 16, namely is radius R_{PNS} , mass M_{PNS} , and magnetic energy E_{PNS} , which we compute as volume integrals over the region where $\rho > 10^{11} \text{ g cm}^{-3}$. Initially, the PNS mass and radius for both models are largely identical until ≈ 0.15 s aside from minimal differences resulting from small differences during the collapse phase. After this point, M_{PNS} continues to grow in the weak-field model and the model maintains a larger R_{PNS} since accretion continues longer than in the strong-field model. The final baryonic masses are $1.63 M_{\odot}$ and $1.69 M_{\odot}$ for the strong- and weak-field model, respectively. Using the approximation of Lattimer & Yahil (1989); Lattimer & Prakash (2001) for the neutron star binding energy, the gravitational mass M_{grav} can be obtained from

$$M_{\text{by}} = M_{\text{grav}} + 0.084 M_{\odot} (M_{\text{grav}} / M_{\odot})^2, \quad (25)$$

which results in $M_{\text{grav}} = 1.46 M_{\odot}$ for the strong-field model and $M_{\text{grav}} = 1.50 M_{\odot}$ for the weak-field model.

The evolution of the interior and surface field of the PNS is of particular interest in the context of magnetar and pulsar birth scenarios. Due to the vast differences in initial magnetic field strength, the initial E_{PNS} (bottom panel of Figure 16) differs by orders of magnitude between the strong- and weak-field models. For the strong-field

model E_{PNS} remains rather steady at 10^{47-48} erg until about 0.25 s after bounce. In the weak-field model, E_{PNS} starts at much smaller values, but gradually grows due to compression of the field lines as the R_{PNS} contracts, shear flows in the PNS surface region, and amplification by PNS convection. Eventually E_{PNS} becomes comparable to the strong-field model about 0.25 s after bounce. It is noteworthy that by the end of the simulation, the magnetic energy in the PNS is dropping in the strong-field model and ends up slightly lower than in the weak-field model. The drop in magnetic energy for the strong-field model is likely due to numerical reconnection and variations in field amplification by PNS convection. While turbulent reconnection is bound to occur in the PNS convection zone, the destruction of magnetic fields may be overestimated numerically, especially at the modest resolution affordable inside the PNS. Nonetheless, the simulations at least strongly indicate that the memory of the initial fields is largely lost inside the PNS.¹

To elucidate the spatial structure of the PNS magnetic field, we plot profiles of the dipole strength of the radial magnetic field and the root-mean-squared average of the total field strength against density for the strong- and weak-field models in Figure 17. The tentative ‘‘surface’’ of the PNS where $\rho = 10^{11} \text{ g cm}^{-3}$ is indicated by dotted vertical line, but it must be borne in mind that further accretion, ablation of surface material by the neutrino-driven wind, and possibly field breakout from the PNS may yet change the PNS surface structure and surface magnetic fields in particular. Just as for the bulk magnetic energy of the PNS, the PNS surface magnetic field has effectively lost memory of the initial condition after less than 0.3 s after bounce, even though the initial magnetic field strengths of both these models were six orders of magnitude apart. At the final simulation time, the surface magnetic field strengths in both models are very similar, with dipole fields of 5×10^{14} G for the weak-field case and 2×10^{14} G for the strong field case. Thus, both models reach magnetar-strength fields at the surface as in previous 3D MHD supernova simulations of non-rotating and slowly-rotating progenitors (Müller & Varma 2020; Matsumoto et al. 2022), at least transiently. It is interesting, however, that the surface field in the strong-field model is decreasing at the end of the simulation, which may reduce possible tensions with the observed field strength distribution of young neutron stars. The declining field strength is consistent with the development of net outflow from the PNS surface, i.e., an incipient neutrino-driven wind, which implies a change from flux compression to flux expansion. The final surface field strength is obviously still beyond the scope of the current simulations.

We next consider the kick velocity and angular momentum of the newly born neutron star, which we plot in Figure 18. Following Scheck et al. (2008), we evaluate the kick indirectly from the momentum of the ejecta assuming angular momentum conservation since the innermost part of our grid is treated in spherical symmetry and does not allow the PNS to move freely. Specifically, we compute

$$\mathbf{v}_{\text{kick}} = -\frac{1}{M} \int_{r > R_{\text{gain}}} \rho \mathbf{v} dV, \quad (26)$$

where M is the total mass² inside the gain radius, and the integral covers the entire volume outside the gain radius. In both models, the

¹ PNS fields originating from field with significant helicity might still be protected better from field decay in the long run, but once PNS convection has died down and differential rotation has been eliminated, field decay will be extremely slow because of the high conductivity of neutron star matter, regardless of the helicity of the field configuration.

² Although the choice between the baryonic and gravitational mass would only make a minor difference here, we note that it is appropriate to use the

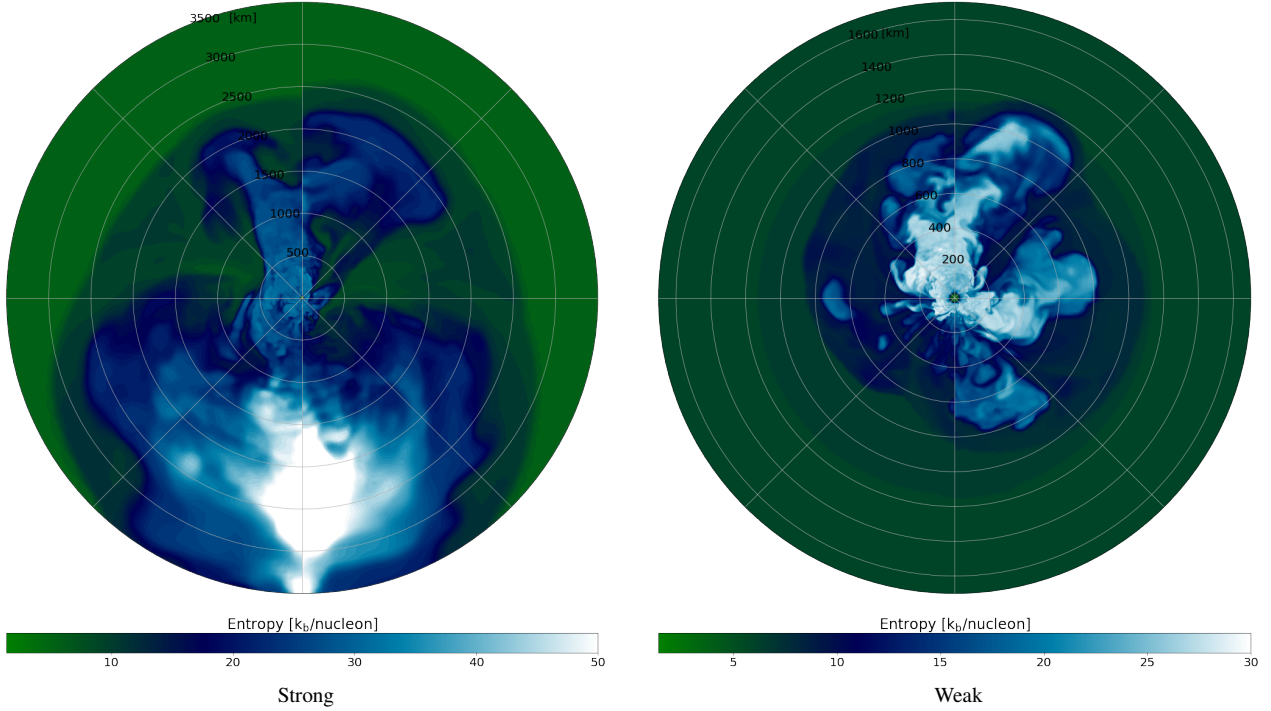


Figure 15. Entropy on meridional slices through the strong (left) and weak-field (right) model at 0.30 s after bounce. The strong-field model has a weakly bipolar explosion geometry with a prominent plume along the South polar axis and a weaker outflow along the North polar axis. The biggest neutrino-heated plume in the weak-field model is also aligned with the axis, but there are smaller plumes in other directions, most notably near the equatorial plane in the 4 o'clock direction.

kick is almost aligned with the z -axis of the spherical polar grid, reflecting the explosion geometry shown in Figure 15, and thus the forcing by initial perturbations and/or the spherical polar grid geometry (cp. discussion in Section 4.2). As expected, the kick points in the direction opposite to the most prominent plume, i.e., towards the North pole in the strong-field model and towards the South pole in the weak-field model, at least by the end of the simulation. Since the explosion in the weak-field model has not yet sufficiently advanced to extrapolate the final value of the kick, which has only reached 84 km s^{-1} by the end of the simulation. The kick direction may also still be subject to change, since other non-grid aligned plumes and downflows are still present in the weak-field model and may impart momentum onto the PNS in other directions. In the strong-field model, the kick reaches 326 km s^{-1} , and although it is still growing, its rate of change is decreasing. Since accretion downflows have already been quenched and the ejecta are expanding steadily, the final kick will only grow further by a modest amount. We can estimate the final kick velocity of these models using the extrapolation method demonstrated in Müller et al. (2019b) to find final PNS kick velocities of 345 km s^{-1} and 110 km s^{-1} for the strong and weak-field simulations, respectively. We thus expect the final kick to lie within the typical range observed for young neutron stars (Hobbs et al. 2005).

The second panel in Figure 18 shows the angular momentum \mathbf{J} of the PNS, which is obtained by integrating the magnetic torques and

baryonic PNS mass for evaluating the kick in a pseudo-Newtonian simulation. Although the inertial mass of the neutron star is eventually reduced by neutrino emission as it cools, near-isotropic emission of neutrinos in the PNS rest frame will not change the PNS velocity, and decrease the PNS momentum proportionately to the decrease in inertial mass.

hydrodynamic angular momentum fluxes onto the PNS in time and over the surface of a sphere of radius 30 km,

$$\frac{d\mathbf{J}}{dt} = - \oint (\mathbf{r} \times \mathbf{v}) \rho v_r dA + \frac{1}{4\pi} \oint (\mathbf{r} \times \mathbf{B}) B_r dA. \quad (27)$$

For the strong-field model, the contribution from magnetic torques is also shown separately. We note, however, that our choice of the PNS surface being at 30 km is somewhat arbitrary; other works such as Wongwathanarat et al. (2013) have used a considerably larger analysis region up to radii of several hundred kilometres. The choice of a small radius is designed to better capture the current PNS spin, but the final spin of the PNS depends rather sensitively on how much of the material in its vicinity is eventually accreted or blown out³. The eventual multi-dimensional “mass cut” cannot be predicted at this rather early stage of the explosion yet. This introduces a significant uncertainty on the final spin, since the shells outside 30 km still carry considerable angular momentum and have not yet been brought into rigid rotation with the PNS by the end of the simulation. Experiments with different analysis radii (corresponding to different hypothetical mass cuts) indicate that the PNS angular momentum could still change by a small factor, with the direction of the spin appearing more uncertain than the spin magnitude. By contrast, \mathbf{v}_{kick} is quite insensitive to the precise choice of the analysis region. The results for the weak-field model are only shown for the sake of completeness; as for the kick, the angular momentum shows no sign

³ The sensitivity of the PNS spin to rather small amounts of accretion has been demonstrated most perspicuously in the extreme case of fallback accretion at later times, which can easily spin up the PNS to millisecond periods (Chan et al. 2018, 2020; Stockinger et al. 2020).

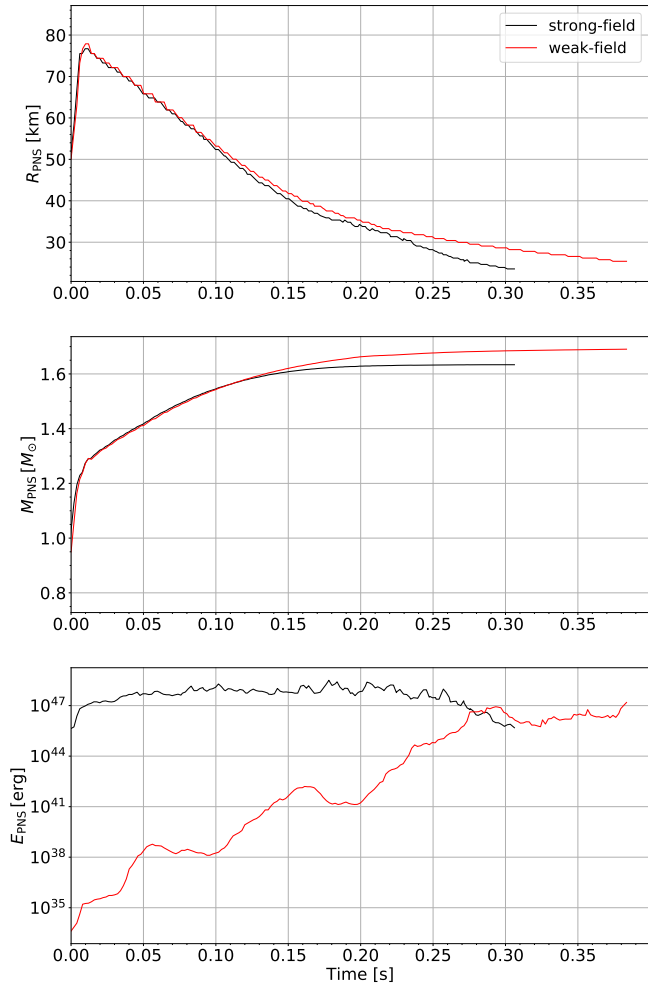


Figure 16. Evolution of the radius R_{PNS} , baryonic mass M_{PNS} , and magnetic energy E_{PNS} of the PNS for the strong-field model (black) and the weak-field model (red). The PNS surface is defined as the radius where the angle-averaged density reaches $10^{11} \text{ g cm}^{-3}$.

of saturation in this case yet. Its absolute value at the end of the simulation is $5.11 \times 10^{45} \text{ g cm}^2 \text{ s}^{-1}$ and is still growing.

In the strong-field model, the angular momentum of the PNS has largely frozen out, however. By the end of the simulation, it has reached about $1.36 \times 10^{47} \text{ g cm}^2 \text{ s}^{-1}$. It is interesting to note that the spin-up of the PNS in the strong-field model is driven mostly by magnetic torques.

Using the analytic approximation for the neutron star moment of inertia from [Lattimer & Schutz \(2005\)](#),

$$I \approx 0.237 M_{\text{grav}} R^2 \left[1 + 4.2 \left(\frac{M_{\text{grav}} \text{ km}}{M_{\odot} R} \right) + 90 \left(\frac{M_{\text{grav}} \text{ km}}{M_{\odot} R} \right)^2 \right], \quad (28)$$

the angular momentum can be translated into a neutron star spin period $P = J/I$. Assuming a final neutron star radius R of 12 km, we estimate the moment of inertia as $1.52 \times 10^{45} \text{ g cm}^3$ for the strong-field model and $1.58 \times 10^{45} \text{ g cm}^3$ for the weak-field model, which corresponds to spin periods of about 73 ms and 1.86 s, respectively. Prima facie, this puts the strong-field model in the range of typical spin-period of young *pulsar* ([Faucher-Giguère & Kaspi 2006](#); [Perna et al. 2008](#); [Popov & Turolla 2012](#); [Igoshev & Popov 2013](#)), and not of magnetars, which are observed to rotate rather slowly ([Olausen & Kaspi 2014](#); [Kaspi & Beloborodov 2017](#)). However, highly mag-

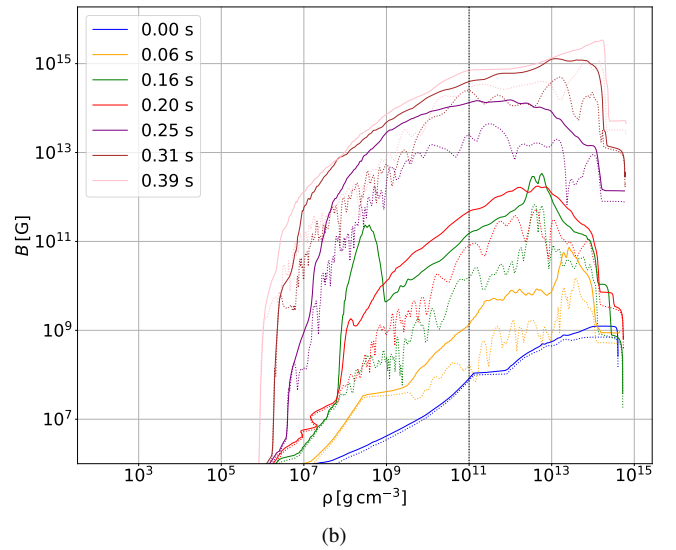
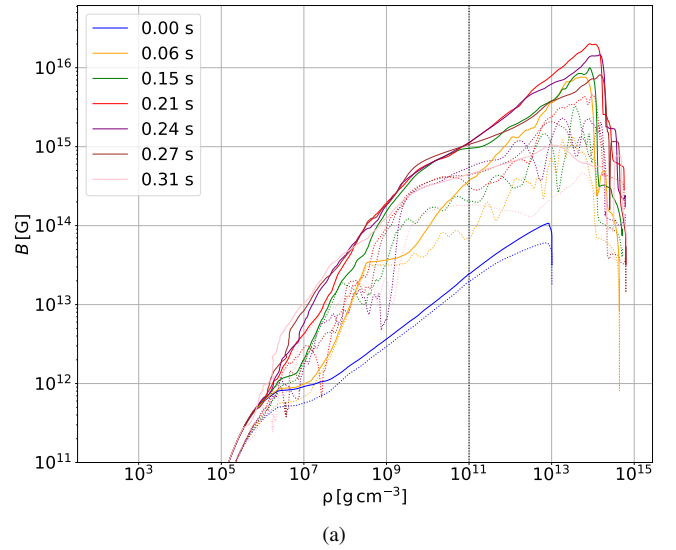


Figure 17. Angle-averaged total magnetic field strength (solid lines, root-mean-square averages), and the dipole component of the radial magnetic field B_r (dotted lines) as a function of density (a) for the strong-field model and (b) for the weak-field model. The vertical dotted black lines indicate the fiducial PNS surface density $\rho = 10^{11} \text{ g cm}^{-3}$.

netised neutron stars will also spin-down rapidly; even the youngest observed magnetars must already have been spun down considerably after the supernovae. We therefore extrapolate the spin period using the neutron star spin-down formula for the period derivative \dot{P} in terms of P and the surface dipole field B_{surf} (cp. [Lorimer & Kramer 2004](#)),

$$\dot{P} = \frac{1}{P} \left(\frac{B_{\text{surf}}}{3 \times 10^{19}} \right)^2 \text{ s}^{-1}. \quad (29)$$

Since the final surface dipole strength is still subject to uncertainties, we calculate the spin-down for several choices of B_{surf} in the range around the tentative dipole field strength of $2 \times 10^{14} \text{ G}$ at the end of our simulation. The extrapolated spin period after several hundred years for the strong-field model (Figure 19) reach several seconds, which is compatible with observations ([Olausen & Kaspi 2014](#)), which show magnetar spin periods of $1 \text{ s} < P < 12 \text{ s}$. The results

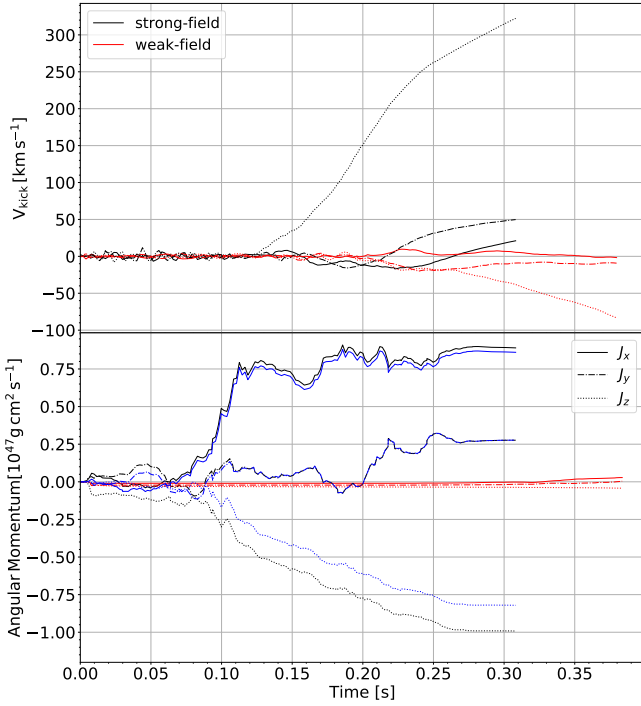


Figure 18. Evolution of the kick and angular momentum of PNS for the strong-field model (black/blue) and the weak-field model (red). For the strong-field model, we show both the time integral of the entire angular momentum flux onto the PNS (black), and the time integral of magnetic torques alone (blue). The advective angular momentum flux and the magnetic torques are evaluated on a sphere of radius 30 km around the origin. Different line styles are used for the three components of the angular momentum vector (solid: J_x , dash-dotted: J_y , dotted: J_z).

can, e.g., be compared to Swift J1818.0–1607 (Blumer & Safi-Harb 2020), one of the youngest known magnetars, which is approximately 500 years old and has a spin period of 1.36 s. For a surface dipole field strength of 10^{14} G, we obtain a spin period of ~ 0.6 s after 500 years. While this is still faster than Swift J1818.0–1607, it is of the same magnitude, and thus appears roughly compatible with observed constraints on magnetar spins, especially considering that stochastic variations among strongly magnetised neutron stars are expected.

Finally, we consider the orientation of the kick and spin direction. Observational evidence has suggested generic spin-kick alignment in neutron stars (Johnston et al. 2005; Noutsos et al. 2012, 2013), but simulations have yet to reveal a robust mechanism for spin-kick alignment; recent attempts to connect spin-kick alignment to rotation (Powell & Müller 2020) or fallback (Janka et al. 2022) have not yielded wholly convincing results. At least during the early explosion phase, magnetic fields in non-rotating supernova models do not appear to provide a mechanism for spin-kick alignment either, as can be seen from Figure 20, which shows the angle α between the spin and kick direction for our models. We find a misalignment of about 50° and 35° at the end of the simulation for the strong- and weak-field models. With supernova explosion models now including magnetic fields, it becomes increasingly difficult to account for spin-kick alignment during the early explosion phase. Spin-kick alignment may indeed be a long-term effect and related, e.g., to later fallback (Janka et al. 2022) (although the mechanism proposed by Janka et al. 2022 likely does not work as intended because of a problem with angular momentum non-conservation).

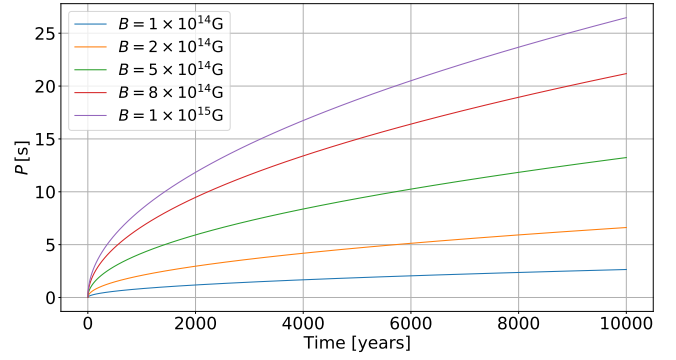


Figure 19. Rotation period of the neutron star as a function of age using the spin-down formula (29).

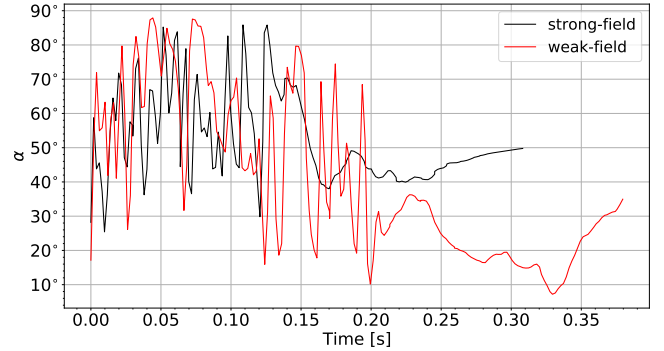


Figure 20. The angle α between the spin and kick directions of the PNS based on an evaluation of the PNS angular momentum using the hydrodynamic fluxes and magnetic torques at a radius of 30 km.

5 CONCLUSIONS

We investigated the role of strong magnetic fields in non-rotating progenitors on core-collapse supernova explosions, specifically its effect on shock revival, explosion dynamics, and the properties of the compact remnant. To this end, we performed 3D simulations of the collapse and explosion of a $16.9 M_{\odot}$ star using a twisted-torus initial field and two different initial field strengths (10^{12} G and 10^6 G at the centre). It has been speculated that strong pre-supernova fields of order 10^{12} G might arise in massive stars as fossil fields from a stellar merger (Ferrario & Wickramasinghe 2005, 2006; Schneider et al. 2019, 2020).

Our simulations show that strong magnetic fields have a noticeable impact on the neutrino-driven explosion mechanism, even in slowly/non-rotating progenitors. The strong-field model undergoes shock revival already early on about 0.1 s after bounce and reaches an explosion energy 9.3×10^{50} erg by the end of our simulation at 0.3 s after bounce. Thus, the model reaches a typical supernova explosion energy faster than in non-magnetised 3D models of core-collapse supernovae from slowly rotating progenitors. While the corresponding weak-field model also explodes somewhat later, it shows a much slower rise of the explosion energy to only 1.2×10^{50} erg by the end of the simulation.

The principal role of magnetic fields in the precipitous and powerful explosion of the strong-field model is to provide an extra boost to neutrino heating and hydrodynamic turbulence to trigger the explosion early, while the explosion is still primarily driven by neutrinos. This is similar to the results of Müller & Varma (2020), who already found that field amplification by a turbulent dynamo can aid shock

revival by the neutrino-driven mechanism; the key difference is that the effect of magnetic fields comes into play early on without the need for an extended growth phase. The saturation field strength in the gain region, corresponding to about 40% of kinetic equipartition is reached almost immediately once neutrino-driven convection develops. In the weak-field model, field amplification by the turbulent dynamo is too slow to have a substantial impact before a neutrino-driven explosion develops

As in Müller & Varma (2020), magnetic fields aid shock revival in the strong-field model by increasing the convective efficiency in the gain region and reducing the binding energy of the gain region. In addition, the strong fields in the progenitor also create sizable perturbations of $\pm 10\%$ in the pre-shock ram pressure, reminiscent of the effect of infalling convective eddies from shell burning in perturbation-aided explosions (Müller & Janka 2015b; Müller et al. 2017; Abdikamalov & Foglizzo 2020). The perturbations are dominated by a large-scale $\ell = 1$ dipole mode. Large-scale ram-pressure perturbations of such amplitudes tend to be strongly conducive to shock revival (Müller & Janka 2015b; Abdikamalov et al. 2016; Huete et al. 2018). In future, the evolution of strong magnetic seed fields in the progenitor and their impact on shock revival need to be investigated using a more consistent approach by basing supernova simulations directly on models of magnetoconvection in massive stars (Varma et al. 2021) and complementing simulations with analytic theory for the amplification and dynamical role of seed perturbations, similar to the hydrodynamic case (Takahashi & Yamada 2014; Müller et al. 2016; Huete et al. 2018; Abdikamalov & Foglizzo 2020; Abdikamalov et al. 2021).

The high explosion energy of the strong-field model is primarily a consequence of early shock revival. Its energetics is consistent with the physics known from other models of neutrino-driven explosions (Marek et al. 2006; Müller 2015; Bruenn et al. 2016; Müller et al. 2017). Nucleon recombination is primarily, but not exclusively, responsible for the delivery of the explosion energy. Due to early shock revival, the volume-integrated neutrino heating rate is high and the specific binding energy of the gain region is modest. These factors allow for a high mass outflow rate, a very efficient conversion of neutrino heating into recombination energy in the ejecta region, and hence a rapid growth of the explosion energy. As in early explosions in 2D simulations (Bruenn et al. 2016), mechanical $P dV$ work and (specific to our model) magnetic stresses also contribute significantly to the energy budget of the ejecta.

The strong-field model has evolved sufficiently far to tentatively extrapolate some properties of the neutron star born in the supernova. Our simulation predicts a gravitational neutron star mass of $1.50M_{\odot}$, a kick velocity of about 345 km s^{-1} , and a birth spin period of about 73 ms. The dipole component of the magnetic field at the surface of the proto-neutron star is about $2 \times 10^{14} \text{ G}$ at the end of the simulation, but is decreasing significantly at this point. Such a field could spin down the neutron star to periods of second within a few hundred years, which would be compatible with the spin period of young magnetars. We do not find spin-kick alignment, and the mechanism that might bring about such an alignment remains opaque.

However, while the raw neutron star parameters from the simulation appear to be quite consistent with observational constraints on young neutron stars and magnetars in particular, our simulations rather prompt more questions about neutron star formation channels and birth properties. It remains unclear whether the proto-neutron star in the strong-field would actually evolve into a magnetar. The surface dipole field strength is decreasing by the end of the simulation, and we cannot follow phenomena that may shape its final magnetic fields on much longer time scales, such as the ablation of surface material

by the neutrino-driven wind, field burial (Romani 1990; Torres-Forné et al. 2016) or breakout of fields from the proto-neutron star convection zone. Regardless of these uncertainties, it is remarkable, though, that the weak-field model actually develops a strong surface dipole field by the end of the simulation than the strong-field model. As far as the proto-neutron star surface field is concerned, memory of the initial conditions appears to be erased within a few hundred milliseconds after collapse. This casts some doubt on the viability of the fossil-field scenario for magnetar formation. Whether amplification and reconnection processes in the supernova core indeed make the neutron star magnetic field independent of the initial field in the long term requires further investigation, however, both because of potential numerical uncertainties (resolution, treatment of the induction equation, etc.) and because the initial field in our simulation was still prescribed by hand. Aside from the question of neutron star surface fields, it is also difficult to square the high explosion energy of the strong-field model with the characteristics of supernova remnants around magnetars, which point to have normal or modest explosion energies (Vink & Kuiper 2006).

Nonetheless, our simulations underscore that it is important to consider the role of magnetic fields in supernova explosions – beyond the more spectacular scenario of magnetorotational supernovae – in order to more fully understand the explosion dynamics and the progenitor-remnant connection. As with hydrodynamic simulations, a more integrated view of magnetic field effects from the progenitor stage to the remnant phase is required for this purpose.

ACKNOWLEDGEMENTS

BM acknowledges support by ARC Future Fellowship FT160100035. This work is based on simulations performed within computer time allocations from Astronomy Australia Limited’s ASTAC scheme, the National Computational Merit Allocation Scheme (NCMAS), and an Australasian Leadership Computing Grant on the NCI NF supercomputer Gadi. This research was supported by resources provided by the Pawsey Supercomputing Centre, with funding from the Australian Government and the Government of Western Australia. This work has received funding from the European Research Council (ERC) under the European Union’s Horizon 2020 research and innovation programme (Grant agreement No. 945806).

DATA AVAILABILITY

The data underlying this article will be shared on reasonable request to the authors, subject to considerations of intellectual property law.

REFERENCES

- Abdikamalov E., Foglizzo T., 2020, *MNRAS*, **493**, 3496
- Abdikamalov E., Zhakyslykov A., Radice D., Berdibek S., 2016, *MNRAS*, **461**, 3864
- Abdikamalov E., Foglizzo T., Mukazhanov O., 2021, *MNRAS*, **503**, 3617
- Aguilera-Dena D. R., Langer N., Antoniadis J., Müller B., 2020, *ApJ*, **901**, 114
- Akiyama S., Wheeler J. C., Meier D. L., Lichtenstadt I., 2003, *ApJ*, **584**, 954
- Balbus S. A., Hawley J. F., 1991, *ApJ*, **376**, 214
- Bisnovaty-Kogan G. S., Popov I. P., Samokhin A. A., 1976, *Ap&SS*, **41**, 287
- Blumer H., Safi-Harb S., 2020, *ApJ*, **904**, L19
- Bollig R., Yadav N., Kresse D., Janka H.-T., Müller B., Heger A., 2021, *ApJ*, **915**, 28
- Braithwaite J., Nordlund Å., 2006, *A&A*, **450**, 1077

- Braithwaite J., Spruit H. C., 2004, *Nature*, **431**, 819
- Bruenn S. W., et al., 2016, *ApJ*, **818**, 123
- Bugli M., Guilet J., Obergaulinger M., Cerdá-Durán P., Aloy M. A., 2020, *MNRAS*, **492**, 58
- Buras R., Janka H. T., Rampp M., Kifonidis K., 2006, *A&A*, **457**, 281
- Burrows A., Dessart L., Livne E., Ott C. D., Murphy J., 2007, *ApJ*, **664**, 416
- Cantiello M., Yoon S. C., Langer N., Livio M., 2007, *A&A*, **465**, L29
- Chan C., Müller B., Heger A., Pakmor R., Springel V., 2018, *ApJ*, **852**, L19
- Chan C., Müller B., Heger A., 2020, *MNRAS*, **495**, 3751
- Colella P., Woodward P. R., 1984, *Journal of Computational Physics*, **54**, 174
- Couch S. M., Chatzopoulos E., Arnett W. D., Timmes F. X., 2015, *ApJ*, **808**, L21
- Dedner A., Kemm F., Kröner D., Munz C. D., Schnitzer T., Wesenberg M., 2002, *Journal of Computational Physics*, **175**, 645
- Donati J.-F., Landstreet J. D., 2009, *ARA&A*, **47**, 333
- Duncan R. C., Thompson C., 1992, *ApJ*, **392**, L9
- Endeve E., Cardall C. Y., Budiardja Mezzacappa A., 2010, *ApJ*, **713**, 1219
- Endeve E., Cardall C. Y., Budiardja R. D., Beck S. W., Bejood A., Toedte R. J., Mezzacappa A., Blondin J. M., 2012, *ApJ*, **751**, 26
- Faucher-Giguère C.-A., Kaspi V. M., 2006, *ApJ*, **643**, 332
- Ferrario L., Wickramasinghe D. T., 2005, *MNRAS*, **356**, 615
- Ferrario L., Wickramasinghe D., 2006, *MNRAS*, **367**, 1323
- Ferrario L., Melatos A., Zrake J., 2016, *Magnetic Field Generation in Stars*. Springer New York, New York, NY, pp 81–113, doi:10.1007/978-1-4939-3550-5_4, https://doi.org/10.1007/978-1-4939-3550-5_4
- Georgy C., Meynet G., Walder R., Folini D., Maeder A., 2009, *A&A*, **502**, 611
- Georgy C., Ekström S., Meynet G., Massey P., Levesque E. M., Hirschi R., Eggenberger P., Maeder A., 2012, *A&A*, **542**, A29
- Grunhut J. H., et al., 2017, *MNRAS*, **465**, 2432
- Gurski K., 2001, in *APS Meeting Abstracts*. p. D2.007
- Heger A., Woosley S. E., Spruit H. C., 2005, *ApJ*, **626**, 350
- Hobbs G., Lorimer D. R., Lyne A. G., Kramer M., 2005, *MNRAS*, **360**, 974
- Huete C., Abdikamalov E., Radice D., 2018, *MNRAS*, **475**, 3305
- Igoshev A. P., Popov S. B., 2013, *MNRAS*, **432**, 967
- Janka H. T., Müller B., Kitaura F. S., Buras R., 2008, *A&A*, **485**, 199
- Janka H.-T., Wongwathanarat A., Kramer M., 2022, *ApJ*, **926**, 9
- Jardine R., Powell J., Müller B., 2022, *MNRAS*, **510**, 5535
- Johnston S., Hobbs G., Vigeland S., Kramer M., Weisberg J. M., Lyne A. G., 2005, *MNRAS*, **364**, 1397
- Kamchatnov A. M., 1982, *Sov. Phys. JETP*, **55**, 69
- Kasen D., Woosley S. E., 2009, *ApJ*, **703**, 2205
- Kaspi V. M., Beloborodov A. M., 2017, *ARA&A*, **55**, 261
- Keane E. F., Kramer M., 2008, *MNRAS*, **391**, 2009
- Lai D., Goldreich P., 2000, *ApJ*, **535**, 402
- Lattimer J. M., Prakash M., 2001, *ApJ*, **550**, 426
- Lattimer J. M., Schutz B. F., 2005, *ApJ*, **629**, 979
- Lattimer J. M., Swesty D. F., 1991, *Nuclear Phys. A*, **535**, 331
- Lattimer J. M., Yahil A., 1989, *ApJ*, **340**, 426
- LeBlanc J. M., Wilson J. R., 1970, *ApJ*, **161**, 541
- Lorimer D. R., Kramer M., 2004, *Handbook of Pulsar Astronomy*. Cambridge Observing Handbooks for Research Astronomers Vol. 4, Cambridge University Press, Cambridge (UK)
- Mabanta Q. A., Murphy J. W., 2018, *ApJ*, **856**, 22
- Makarenko E. I., Igoshev A. P., Kholtygin A. F., 2021, *MNRAS*, **504**, 5813
- Marek A., Dimmelmeier H., Janka H. T., Müller E., Buras R., 2006, *A&A*, **445**, 273
- Masada Y., Takiwaki T., Kotake K., 2015, *ApJ*, **798**, L22
- Matsumoto J., Takiwaki T., Kotake K., Asahina Y., Takahashi H. R., 2020, *MNRAS*, **499**, 4174
- Matsumoto J., Asahina Y., Takiwaki T., Kotake K., Takahashi H. R., 2022, *arXiv e-prints*, p. [arXiv:2202.07967](https://arxiv.org/abs/2202.07967)
- Mestel L., 1999, *Stellar magnetism (International Series of Monographs on Physics; 99)*. Clarendon Press Oxford
- Mestel L., 2001, in Mathys G., Solanki S. K., Wickramasinghe D. T., eds, *Astronomical Society of the Pacific Conference Series Vol. 248, Magnetic Fields Across the Hertzsprung-Russell Diagram*. p. 3
- Meynet G., Eggenberger P., Maeder A., 2011, *A&A*, **525**, L11
- Miyoshi T., Kusano K., 2005, *Journal of Computational Physics*, **208**, 315
- Moss D., 2001, in Mathys G., Solanki S. K., Wickramasinghe D. T., eds, *Astronomical Society of the Pacific Conference Series Vol. 248, Magnetic Fields Across the Hertzsprung-Russell Diagram*. p. 305
- Mösta P., Ott C. D., Radice D., Roberts L. F., Schnetter E., Haas R., 2015, *Nature*, **528**, 376
- Müller B., 2015, *MNRAS*, **453**, 287
- Müller E., Hillebrandt W., 1979, *A&A*, **80**, 147
- Müller B., Janka H. T., 2015a, *MNRAS*, **448**, 2141
- Müller B., Janka H. T., 2015b, *MNRAS*, **448**, 2141
- Müller B., Varma V., 2020, *MNRAS*, **498**, L109
- Müller B., Viallet M., Heger A., Janka H.-T., 2016, *ApJ*, **833**, 124
- Müller B., Melson T., Heger A., Janka H.-T., 2017, *MNRAS*, **472**, 491
- Müller B., et al., 2019a, *MNRAS*, **484**, 3307
- Müller B., et al., 2019b, *MNRAS*, **484**, 3307
- Murphy J. W., Mabanta Q., Dolence J. C., 2019, *MNRAS*, **489**, 641
- Noutsos A., Kramer M., Carr P., Johnston S., 2012, *MNRAS*, **423**, 2736
- Noutsos A., Schnitzler D. H. F. M., Keane E. F., Kramer M., Johnston S., 2013, *MNRAS*, **430**, 2281
- Obergaulinger M., Aloy M. A., 2021, *MNRAS*, **503**, 4942
- Obergaulinger M., Cerdá-Durán P., Müller E., Aloy M. A., 2009, *A&A*, **498**, 241
- Obergaulinger M., Janka H. T., Aloy M. A., 2014, *MNRAS*, **445**, 3169
- Olausen S. A., Kaspi V. M., 2014, *ApJS*, **212**, 6
- Perna R., Soria R., Pooley D., Stella L., 2008, *MNRAS*, **384**, 1638
- Petrovic J., Langer N., Yoon S. C., Heger A., 2005, *A&A*, **435**, 247
- Popov S. B., Turolla R., 2012, *Ap&SS*, **341**, 457
- Powell J., Müller B., 2020, *MNRAS*, **494**, 4665
- Quentin L. G., Tout C. A., 2018, *MNRAS*, **477**, 2298
- Rampp M., Janka H. T., 2000, *ApJ*, **539**, L33
- Raynaud R., Guilet J., Janka H.-T., Gastine T., 2020, *Science Advances*, **6**, eaay2732
- Romani R. W., 1990, *Nature*, **347**, 741
- Sawai H., Yamada S., Suzuki H., 2013, *ApJ*, **770**, L19
- Scheck L., Janka H. T., Foglizzo T., Kifonidis K., 2008, *A&A*, **477**, 931
- Schneider F. R. N., Ohlmann S. T., Podsiadlowski P., Röpke F. K., Balbus S. A., Pakmor R., Springel V., 2019, *Nature*, **574**, 211
- Schneider F. R. N., Ohlmann S. T., Podsiadlowski P., Röpke F. K., Balbus S. A., Pakmor R., 2020, *MNRAS*, **495**, 2796
- Schneider F. R. N., Podsiadlowski P., Müller B., 2021, *A&A*, **645**, A5
- Schöller M., et al., 2017, *A&A*, **599**, A66
- Spruit H. C., 2009, in Strassmeier K. G., Kosovichev A. G., Beckman J. E., eds, *IAU Symposium Vol. 259, Cosmic Magnetic Fields: From Planets, to Stars and Galaxies*. pp 61–74, doi:10.1017/S1743921309030075
- Stockinger G., et al., 2020, *MNRAS*, **496**, 2039
- Suijs M. P. L., Langer N., Poelarends A. J., Yoon S. C., Heger A., Herwig F., 2008, *A&A*, **481**, L87
- Takahashi K., Yamada S., 2014, *ApJ*, **794**, 162
- Thompson C., Duncan R. C., 1993, *ApJ*, **408**, 194
- Torres-Forné A., Cerdá-Durán P., Pons J. A., Font J. A., 2016, *MNRAS*, **456**, 3813
- Tricco T. S., Price D. J., Bate M. R., 2016, *Journal of Computational Physics*, **322**, 326
- Varma V., Müller B., 2021, *MNRAS*, **504**, 636
- Varma V., Müller B., Obergaulinger M., 2021, *Monthly Notices of the Royal Astronomical Society*, **508**, 6033
- Vink J., Kuiper L., 2006, *MNRAS*, **370**, L14
- Wieczorek M., Mmesch de Andrade E. S., Oshchepkov I., heroxbd 2016, *SHTOOLS/SHTOOLS: Version 4.0*, doi:10.5281/zenodo.206114, <https://doi.org/10.5281/zenodo.206114>
- Wongwathanarat A., Janka H.-T., Müller E., 2013, *A&A*, **552**, A126
- Woods P. M., 2008, in Bassa C., Wang Z., Cumming A., Kaspi V. M., eds, *American Institute of Physics Conference Series Vol. 983, 40 Years of Pulsars: Millisecond Pulsars, Magnetars and More*. pp 227–233, doi:10.1063/1.2900149
- Woosley S. E., Bloom J. S., 2006, *ARA&A*, **44**, 507
- Woosley S. E., Heger A., 2006, *ApJ*, **637**, 914

This paper has been typeset from a \TeX/L\AA\TeX file prepared by the author.